Part II

Transport of inertial particles under the action of sea waves

"Make a model as simple as possible, but not simpler."

– Albert Einstein

List of Symbols

d^2	absolute dispersion
$\mathscr{R}$	auto-correlation function
CSF	Corey shape factor
w_s^D	Dietriech settling velocity
D	diffusion coefficient
β	dimensionless added-mass
w_s^m	experimental net settling velocity
σ	frequency
F_r	Froude number
T	integral scale
w_s^*	non dimensional settling velocity
ρ_p	particle density
d_p	particle diameter
R_p	particle Reynolds number
$g^{'}$	reduced gravity acceleration
R	reflection coefficient
w_s	settling velocity
$\boldsymbol{R}$	stochastic noise
S_t	Stokes number
τ	Stokes response time
a	wave amplitude
ω	wave angular frequency

c	wave celerity
H	wave height
k	wave number
T	wave period
λ	wavelength if not stated otherwise

CHAPTER 7

INTRODUCTION

The marine environment is continuously and increasingly threatened with pollution derived from anthropogenic activities, through the uncontrolled released of waste and dangerous substances transported by winds and rivers from land to sea. Among these, the presence of plastics, at different sizes, is now recognized as one of the main threats to the whole environment (Villarrubia-Gómez et al., 2018). Its global production has increased significantly over the past decades, reaching more than 348 million tonnes in 2017, see for example the Annual Report issued by the Association PlasticsEurope (PlasticsEurope, 2018). A widely accepted definition of Microplastics (MPs) requires plastic particles to be smaller than 5 mm in size (Hidalgo-Ruz et al., 2012). However, a clear and accepted terminology and classification is still under discussion (Hartmann et al., 2019) as well as a standardization of the plastic collection and analysis methods (Cutroneo et al., 2020). Besides the dimension, it is important to note that MPs mass densities are generally close to that of water but may be either positively or negatively buoyant (Hidalgo-Ruz et al., 2012; Kooi and Koelmans, 2019). The mass density depends primarily on the plastic composition, with a wide range of values (e.g. high density polyethylene, 930 - 970 $kg.m^{-3}$, polypropylene, 850 - 920 $kg.m^{-3}$, polyvinyl chloride, 1300 - 1450 $kg.m^{-3}$), that can be further modified in the marine environment by degradation or colonization of biofouling and weathering processes (Kaiser et al., 2017; Kooi et al., 2017;

Porter et al., 2018). These aspects play a fundamental role on the fate of plastic debris in the environment primarily influencing the settling velocity of the plastic particles. Several studies have been dedicated to the accurate estimation of the settling velocities depending on the main physical properties of the particles, namely size, shape and density (Chubarenko et al., 2016; Khatmullina and Isachenko, 2017; Waldschlager and Schuttrumpf, 2019).

A great effort has been devoted in these last ten years in quantifying the plastics (micro and macro) abundance in the different compartments (surface water, water column and sediment) of open seas and other delicate environments (coastal areas, estuaries and rivers), see among others Hidalgo-Ruz et al. (2012), Law (2017) and Rezania et al. (2018) for comprehensive reviews. The main outcome of these studies was that plastics in different form (floating debris, microplastic pieces and plastic fibers) are found in any sea basin around the world, with higher concentrations occurring in areas characterized by intense human activity. Recent field campaign found a non negligible plastics content even in the most remote sea basins (Bergmann et al., 2017; Suaria et al., 2020). This demonstrates that plastic debris transport can be extremely efficient and that the prediction of the plastics fate is of paramount importance. The plastics dispersion is driven by a number of physical processes, acting over a wide range of scales; it is worth mentioning the predominant effects of oceanic and coastal currents, wind and sea wave transport through the Stokes drift.

Most efforts to numerically model MPs transport in the ocean or coastal areas treat the particles as neutrally buoyant tracers (Maximenko et al., 2012; Ballent et al., 2013; Zambianchi et al., 2017). Other models include effects related to wind-induced mixing and a superimposed constant settling velocity (Kukulka et al., 2012; Isobe et al., 2014; Kukulka and Brunner, 2015; Brunner et al., 2015; Liubartseva et al., 2016; Zhang, 2017; Kooi et al., 2017; Liubartseva et al., 2018). Overall, most of the classical approaches in MP dispersion substantially disregard inertial effects owing to buoyancy and drag. Recent contributions have been devoted to fill this gap in understanding the role of inertial character of heavy particles, using more refined models to describe the particle trajectories. The transport of heavy particles has attracted the attention of scientists in the last decades, owing to the wide range of applications in both industrial and environmental flows. A great effort has been dedicated to understand how homogeneous turbulence or turbulent

boundary layers are able to transport particles at different scales. The inertial character of the particles proved to modify substantially the statistics of the particle velocity and acceleration fluctuations (Bec et al., 2006, 2007; Cencini et al., 2006) and the shape of the auto-correlation functions and the corresponding integral scales (Ayyalasomayajula et al., 2006; Gerashchenko et al., 2008; Wetchagarun and Riley, 2010). One of the interesting consequences of the modified velocity auto-correlation functions is the effect on the dispersion regimes that heavy particles show (Jung et al., 2008; Wetchagarun and Riley, 2010; Zhang and Xiao, 2018).

Fluid particles immersed in a turbulent flow tend to behaves differently from their fluid counterpart and this is often investigated using the auto-correlation functions and the flow properties of the *fluid seen by particles* (Pozorski and Minier, 1998, 1999; HE et al., 2006; Jung et al., 2008). Inertial particles were found to behave differently from fluid particles already for Stokes number of order one and their typical Lagrangian integral scales is extremely sensitive to the values of the Stokes number (Jung et al., 2008).

A great amount of studies are dedicated to the interaction of heavy particles with turbulent flows (boundary layers or homogeneous turbulence) and channel flows showing interesting processes of clustering (Weiss et al., 2019; Fong et al., 2019; Barge and Gorokhovski, 2020; Berk and Coletti, 2021; Baker and Coletti, 2021).

On the other hand, gravity effects on heavy particles transport received less attention, even if they play a determinant role in several geophysical context, e.g. in atmospheric transport (Yudine, 1959; Csanady, 1963; Wang and Stock, 1993; Shao, 1995; Gustavsson and Mehlig, 2016; Berk and Coletti, 2021). One of the main results of the mentioned studies is that the diffusion theory by Taylor (1921) proved to be valid, provided a correct definition of the decorrelation time is used, even for fairly high values of the Stokes number. In particular, a diffusive regime was observed numerically and experimentally leading to diffusion coefficients that can be lower or higher with respect to the fluid ones depending on the Stokes number (Yudine, 1959; Jung et al., 2008). After introducing a wide class of models of inertial particle dynamics, we analyzed several particular cases, starting from the Basset-Buossinesq-Oseen equation and the Maxey-Riley equationMaxey and Riley (1983) to describe the inertial particle trajectories and the resulting Taylor's formulas in simplified cases (buoyancy-force case, Brownian force case, limiting cases for the Stokes number).

In this chapter, we show the experimental investigation on the inertial Stokes drift depending on several controlling parameters, i.e. wave and particle characteristics. The results will be used to validate previous models and, ultimately, to suggest a new analytical formulation of the net settling velocity to describe MPs transport in wave-exposed environments. Moreover, we also investigated the possibility that the transport of inertial particles owing to sea waves could be described in terms of an asymptotic diffusive regime. Thus, in the second part of the chapter, we provide a simplified transport model based on the Maxey and Riley's equations (Maxey and Riley, 1983), including the effect of a background random flow disturbances superimposed to the wave field. The inclusion of a stochastic term proportional to a diffusion coefficient is a common simplified model to consider an isotropic random force acting on the particle (Reeks, 1988; Boi et al., 2018; Rosti et al., 2020). The main application is the transport of negatively buoyant microplastic particles. The choice of the range of the main particle parameters is guided by several studies of observations of micro-plastics sampled both in the water column and in the sea bed sediment. In a recent statistical analysis, Kooi and Koelmans (2019) analyzed the data from many field studies and provided a description in terms of multi-dimensional probability functions. We rely on the cited work for the definition of the range of particle diameters and the density of the inertial particle. Moreover, sea waves parameters are varied with the aim to understand the role of the intensity of the Stokes drift.

After a brief introduction of the experimental set up and methods and a mathematical background of the numerical approach, a section dedicated to the experimental and numerical results is provided. A conclusive section is reported in the end.

CHAPTER 8

METHODS

8.1 EXPERIMENTAL METHODS

8.1.1 EXPERIMENTAL SETUP

The experiments were performed in the MIO/SEATECH wave flume at SEATECH Engineering School, University of Toulon. The flume is 13 m long, 30 cm wide and 50 cm deep. The net length of the flume that can be used for experimental measurements is about 10 m. The flume is equipped with a piston wave-maker with a pneumatic actuator, remotely controlled using a digital signal acquisition/generation system. The flume side walls are made of thick glass panel allowing for direct visualization and video recordings. For the present experiments the water depth was kept constant and equal to 26.5 cm. A dissipative sloping beach was installed at the end of the flume to minimize the effects of wave reflection. Regular waves were imposed with variable period and amplitude. During each experiment, the generated wave field was monitored using three wave gauges (sampling frequency 200 Hz), placed in the center line of the flume at 1, 2.22 and 2.64 m downstream the wave maker. The wave gauge data have been analysed in order to compute the wave characteristics (period and amplitude) through peak analysis and to quantify the reflection at the dissipative beach following the three gauges method (Drevard et al., 2009; Rey et al., 2002). A schematic overview of the experimental set up is shown

in Figure 8.1.

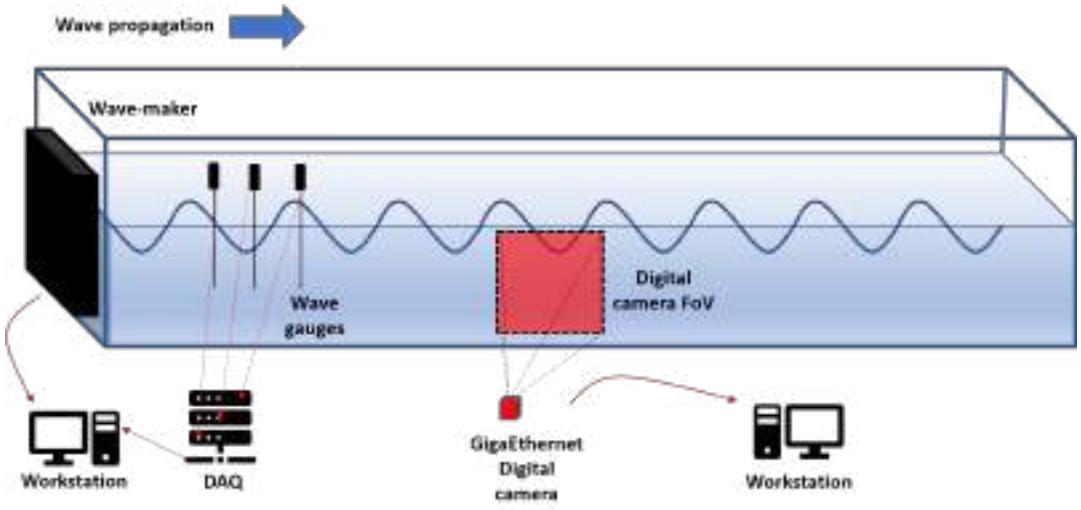

Figure 8.1: Schematic view of the experimental set up

The recovered wave data for the five wave cases are summarized in Table 8.1. The dimensionless parameter H/gT^2 is employed to synthetically describe a sea state, see LeMéhauté (1969). It can also be viewed as a measure of wave steepness: for a given wave period T, higher values of H/gT^2 correspond to higher and steeper waves, since the wave period is related to the wave length through the dispersion relationship. The set of waves generated in the present experimental campaign is such that the wave parameter H/gT^2 is monotonically increasing moving from the first wave condition (W1) to the last one (W4). Overall, the experimental values of H/gT^2 are in a realistic range and they can well represent typical sea state conditions of several sea basins Stocchino et al. (2019). All waves conditions fall in the intermediate depth regime except for W1 that correspond to shallow water conditions. The reflection coefficient ranges between 0.16 and 0.23, which means that the reflection effect is quite small.

Wave Condition	H [m]	T [s]	R	H/gT^2	Exp.#
W1	0.031	0.85	0.23	0.0044	7-12
W2	0.041	0.85	0.16	0.0058	13-18
W3	0.077	0.85	0.17	0.0108	19-24
W4	0.033	0.5	0.18	0.0134	25-30

Table 8.1: Measured wave conditions. The reflection coefficient R has been evaluated following Drevard et al. (2009). The last column refers to the experiment number given Table 8.3

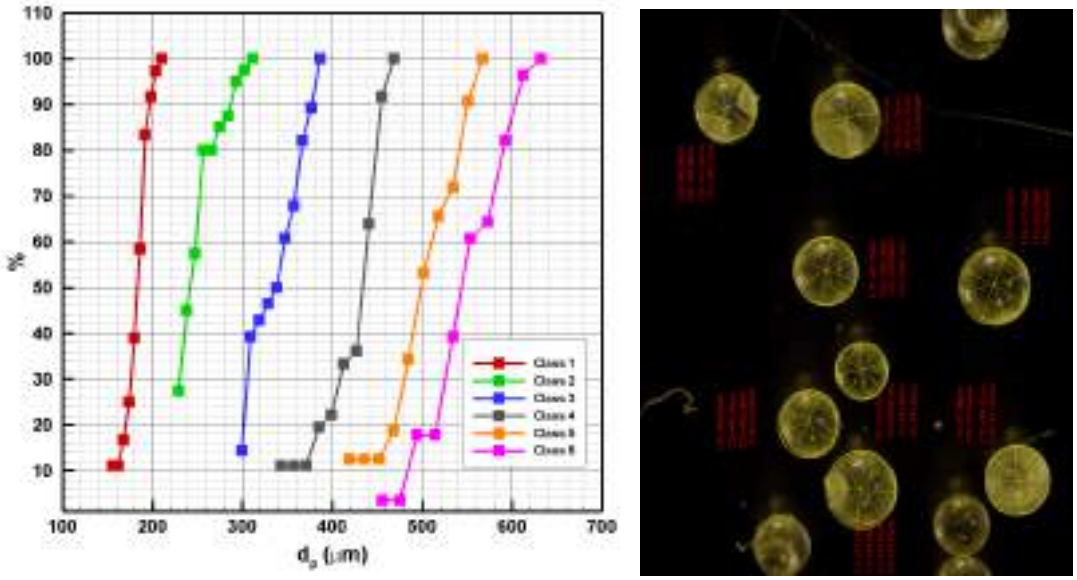

Figure 8.2: left panel: Particle diameter distributions for the six selected classes. Right panel: example of microscope images with the particle diameter measurements

8.1.2 PARTICLES

The selected PMMA (polymethylmetacrylate) particles have a fixed density $\rho_p = 1190\ kg.m^{-3}$ and different diameters d_p ranging from 150 and 640 μm. The PMMA particles were initially sold as a mixture with a poorly sorted grain size distribution. The particles were, therefore, previously sieved to obtain six grain classes with narrow size distributions, see Figure 8.2.

The particle diameters have been evaluated using microscope imaging analyzed with a specific software (open source software ImageJ, imagej.nih.gov). Size statistics for the six selected classes are reported in Table 8.2. A particle diameter distribution is defined starting from a list of diameter sizes within the selected sieve. Than, they are ranged and normalized by the total amount of the sampled diameters. The d_x diameter is the diameter at which x% of particles are finer and (100-x)% of particles are coarser. The resulting size distributions are narrow enough to consider the d_{50} diameter as representative of the PMMA particle diameter, simply named d_p in the following. Plastic particles have been characterized in terms of their added-mass represented by the dimensionless parameter β, and their drag response through the Stokes response time τ,

class	d_{16} (μm)	d_{50} (μm)	d_{84} (μm)
1	512	543	574
2	468	498	528
3	417	433	451
4	307	338	368
5	217	241	267
6	173	183	193

Table 8.2: Main parameters for the six selected classes of PMMA particles.

defined as:

$$\beta = \frac{3\rho_f}{\rho_f + 2\rho_p} \tag{8.1}$$

$$\tau = \frac{d_p^2}{12\beta\nu} \tag{8.2}$$

where ρ_f and ρ_p are the density of the fluid, water in the present case, and the particle, respectively and, ν is the kinematic viscosity of the water. For the present experiments, the added-mass parameter β kept a constant value equal to 0.8876. Note that the well known Stokes number can be readily evaluated as

$$S_t = \omega\tau \tag{8.3}$$

where $\omega = 2\pi/T$ is the angular frequency of the waves.

8.1.3 TEST CASES

A total of 30 experiments have been performed. The main experimental parameters (wave and particles) are reported in Table 8.3. Four different wave conditions were tested by varying period and amplitude, see Table 8.1 for further details. For each wave condition, all particle classes have been released and tested. Experiments from 1 to 6 (not reported in Table 8.3) were dedicated to the experimental protocol testing and therefore not considered for the physical analysis. For each experiment, the particles of a specific diameter class have been released manually at the free surface, few millimetres below it to avoid surface tension effects. The release was repeated several times during a single acquisition in order to increase the number of measured trajectories.

exp	d_p [μm]	T [s]	H [m]	τ	S_t
007	543	0.85	0.031	0.029	0.214
008	498	0.85	0.031	0.024	0.177
009	433	0.85	0.031	0.017	0.127
010	338	0.85	0.031	0.011	0.079
011	241	0.85	0.031	0.006	0.044
012	183	0.85	0.031	0.003	0.023
013	543	0.85	0.041	0.029	0.214
014	498	0.85	0.041	0.024	0.177
015	433	0.85	0.041	0.017	0.127
016	338	0.85	0.041	0.011	0.079
017	241	0.85	0.041	0.006	0.044
018	183	0.85	0.041	0.003	0.023
019	543	0.85	0.077	0.029	0.214
020	498	0.85	0.077	0.024	0.177
021	433	0.85	0.077	0.017	0.127
022	338	0.85	0.077	0.011	0.079
023	241	0.85	0.077	0.006	0.044
024	183	0.85	0.077	0.003	0.023
025	543	0.5	0.033	0.029	0.363
026	498	0.5	0.033	0.024	0.302
027	433	0.5	0.033	0.017	0.216
028	338	0.5	0.033	0.011	0.135
029	241	0.5	0.033	0.006	0.075
030	183	0.5	0.033	0.003	0.040

Table 8.3: Experimental wave and particles parameters.

8.1.4 SETTLING TRAJECTORY MEASUREMENTS

The present measurement strategy was specifically designed to track the trajectories of settling particles under the influence of waves. The particle motion were recorded by a high-definition GigaEthernet digital camera (Teledyne Dalsa Genie Nano C2450) with a 25mm lens. The camera CCD is a 2/3$''$ format with a resolution of 2448×2048 pixel. The frame rate was adjusted for each experiment, ranging between 20 and 25 fps. The camera optical axis was kept orthogonal to the flume glass wall. The field of view (FoV) was about 22×28 cm, allowing to visualize the entire flow depth and the horizontal movements of the settling particles. The illumination of the FoV has been obtained using four 500 W white light halogen lamps complemented, in some cases, with a 200 mW solid state laser.

A single acquisition typically lasted between 100 and 200 s, producing between 2500 and

4000 images depending on the frame rate. A systematic background removal was applied on each image to eliminate spurious reflections and regions with non uniform illumination. The resulting images were then binarized applying a proper threshold based on the image intensity to ease subsequent analysis.

The processed images were analysed using the tracking software MotionStudio^{TM} (Integrated Design Tool, Inc). The tracking procedure started manually by indicating the features that the software shall track in the image sequence and setting a small area around the interested particle, namely an Interrogation Window (IW). The tracking algorithm is based on a cross-correlation of the IW between successive pairs. The above procedure has been applied many times on the same image sequence in order to obtain a statistically significant set of particle trajectories. In general, for each experiment, we have obtained a variable number of single particle trajectories between 30 and 60 depending on the quality of the images: diameters lower than 300 μm were generally more difficult to track, owed to both the size and a lack of proper illumination. In fact, based on the field of view of the images and the resolution of the digital camera, a single pixel represents about 100 μm. Particle with diameters smaller than 300 μm becomes comparable with the pixel size and, then, their tracking is impossible. In order to overcome this limitation, both increasing the digital camera resolution or decreasing the field of view would enable the tracking of this class of particles. The present method is similar to the Particle Image Velocimetry technique used in a recent study (Waldschlager and Schuttrumpf, 2019).

8.2 Numerical Methods

8.2.1 Mathematical model and numerical experiments

The Eulerian wave flow on a vertical plane (x,z), $\mathbf{u}(\mathbf{x},t) = (u_x(\mathbf{x},t); u_z(\mathbf{x},t))$ is calculated assuming a second order Stokes wave as Dean and Dalrymple (1991):

$$\begin{cases} u_x(x,z,t) = \left(\dfrac{gka}{\omega}\right) f_{c1} \cos(kx-\omega t) + \left(\dfrac{g(ka)^2}{\omega}\right) f_{c2} \cos 2(kx-\omega t), \\ u_z(x,z,t) = \left(\dfrac{gka}{\omega}\right) f_{d1} \sin(kx-\omega t) + \left(\dfrac{g(ka)^2}{\omega}\right) f_{d2} \sin 2(kx-\omega t), \end{cases} \tag{8.4}$$

where g is the gravitational acceleration, a is the wave amplitude, $k = 2\pi/\lambda$ is the wave number and λ the wavelength, $\omega = 2\pi/T$ is the angular frequency with T the wave period. The wavenumber

k and the angular frequency ω are linked by a dispersion relation as:

$$\omega = kU_0 + \sigma \tag{8.5}$$

where U_0 is the value of a possible background uniform current velocity and σ is the frequency of the wave in the moving frame of reference (Peregrine, 1976). For the present analysis we did not consider any background flow U_0.

The functions f_{c1}, f_{c2}, f_{d1} and f_{d2} are hyperbolic functions of the water depth h and the vertical coordinate z and read:

$$f_{c1} = \cosh(ks)/\cosh(kz); \tag{8.6}$$

$$f_{c2} = 3\cosh(2ks)/4\sinh^3(kz)\cosh(kh); \tag{8.7}$$

$$f_{d1} = \sinh(ks)/\sinh(kz); \tag{8.8}$$

$$f_{d2} = 3\sinh(2ks)/4\sinh^3(kz)\cosh(kh), \tag{8.9}$$

having defined s as $(h+z)$.

In the following, different waves are described in terms of the wave steepness parameter (Stocchino et al., 2019) defined as H/gT^2, where $H = 2a$, or the Froude number

$$F_r = \frac{\omega a}{c}, \tag{8.10}$$

where c is the wave celerity (Santamaria et al., 2013).

The motion of a small spherical inertial particle can be described by a set of equations that reads:

$$\begin{cases} \dfrac{d\mathbf{x}(t)}{dt} = \mathbf{u}^p(t) + \sqrt{2D}\,\mathbf{R}(t), \\ \dfrac{d\mathbf{u}^p(t)}{dt} = \dfrac{\mathbf{u}(\mathbf{x},t) - \mathbf{u}^p(t)}{\tau} + (1-\beta)\mathbf{g} + \beta\dfrac{d\mathbf{u}(\mathbf{x},t)}{dt}, \end{cases} \tag{8.11}$$

where $\mathbf{u}^p(t)$ is the Lagrangian particle velocity, $\mathbf{u}(\mathbf{x},t)$ is the flow field acting on the particle derived from equations (8.4), with β, $\tau$and the Stokes number S_t defined by 8.2, 8.2 and 8.3, respectively.

This model is a modified version of the original set of equations of Maxey and Riley (1983) for a spherical particle. In particular, we neglect the Faxen and Basset terms from the original equations similarly to previous studies (Santamaria et al., 2013; DiBenedetto et al., 2018; Stocchino

et al., 2019). Moreover, differently from the original set of equations, in the present context, we included a zeroth-order Markov model term in the first equation. With this simple model a stochastic noise is added to the particle positions through the term $\mathbf{R}(t)$, that assumes random values with zero mean and unitary variance. The *Brownian* motion generated is multiplied by a *diffusion* coefficient D, which should synthetically describe the presence of an external Brownian force per unit mass equal to (Reeks, 1988; Boi et al., 2018)

$$\frac{\sqrt{2D}}{\tau}\mathbf{R}(t). \tag{8.12}$$

It could also be interpreted as the effect of the unresolved turbulent flow scales on single inertial particles (Boi et al., 2015; Van Sebille et al., 2018; Rosti et al., 2020). In our analysis, the coefficient D is used as a free parameter, varied in a range between the molecular diffusion value ($10^{-6}\mathrm{m}^2\mathrm{s}^{-1}$) and a value of $10^{-1}\mathrm{m}^2\mathrm{s}^{-1}$. The inclusion of a Brownian term was used in several previous studies focused on the transport of inertial particles or droplets immersed in different flow fields (Reeks, 1988; Drossinos and Reeks, 2005; Boi et al., 2015, 2016, 2018; Rosti et al., 2020).

We acknowledge that this is a quite crude representation of the influence of possible small scale turbulence effects. However, the particular flow under investigation, namely the flow field generated by a sea wave, is usually characterized by low turbulent intensities, quite different from classical turbulent flows used in other context where the transport of inertial particles has been studied.

The Lagrangian transport equations (8.11) were numerically solved using a fourth order Runge-Kutta method with a fixed integration time step much smaller than the Stokes time. Care must be taken on the choice of the integration time in order to resolve time scales of the order of τ, in our analysis we set the integration time as $\Delta t = \tau/30$.

To investigate the possible dispersive regimes, we designed several series of numerical experiments varying the main physical parameters. In particular, four series of experiments were performed varying the wave parameter H/gT^2 in a range between 0.001 and 0.006 (F_r = $0.02-0.12$). All simulations were performed in deep water conditions. For each wave condition, the particle diameter was varied in a range between 10^2 and 10^3 μm maintaining a fixed value of

test #	d_p [μm]	a [m]	ω [Hz]	H/gT^2	λ [m]	β	τ [s]	S_t	D [m^2/s]	n. sim.
000	100-1000	0.18	1.05	0.001	56.21	0.968	0.00086-0.086	0.0009-0.09	10^{-6}-10^{-1}	114
001	100-1000	0.36	1.05	0.002	56.21	0.968	0.00086-0.086	0.0009-0.09	10^{-6}-10^{-1}	114
002	100-1000	0.71	1.05	0.004	56.21	0.968	0.00086-0.086	0.0009-0.09	10^{-6}-10^{-1}	114
003	100-1000	1.06	1.05	0.006	56.21	0.968	0.00086-0.086	0.0009-0.09	10^{-6}-10^{-1}	114

Table 8.4: Wave and particle parameters used for the numerical simulations.

the added-mass parameter β equal to 0.9677. The resulting values of the Stokes number cover a range approximately between 0.0009-0.09.

8.2.2 Test Cases

A total of 456 simulations were performed using 3500 numerical particles, released at the free surface, for an integration time equal to 1500-3500 wave periods, depending on S_t. The duration of the simulation is chosen in order to let the particles reach a depth where the Stokes drift is no longer felt. The main parameters of the numerical simulations are reported in Table 8.4.

Finally, it is worth discussing the range of particle parameters used for the present study. Since the main application that stimulated the investigation is the transport of microplastic and the role of the sea wave Stokes drift, we selected the range of particles diameters and the values of the relative density using the data analysis reported in two recent reviews on sampled microplastic debris, namely Hidalgo-Ruz et al. (2012) and Kooi and Koelmans (2019).

Hidalgo-Ruz et al. (2012) reviewed 68 studies with the aim to summarize the range of particle debris in terms of sizes and densities. Based on similar data sets, Kooi and Koelmans (2019) suggested a statistical interpretation of the data using multidimensional probability density functions (pdf) involving size, density and shapes (Corey shape factor, CSF (Khatmullina and Isachenko, 2017)) of the debris. In particular, the distribution of plastic density is well fitted by a Normal-Inverse Gaussian distribution with a central value of around 1000 kg/m^3 and a marked positive skewness with non negligible probability values up to 1600 kg/m^3. From this analysis almost half of the observed plastic debris have a density in a range between 960 and 1580 kg/m^3, see the data of their Figures S1 and S4 and Table S3. Using the range of wave parameter reported in Table 8.4, the Stokes number used for the present numerical experiments well describes a wide range of microplastic debris observed in the field.

We acknowledge that assuming a spherical shape is quite a crude representation of the real microplastic debris, since microplastic debris show a Corey shape factor distribution dominated by fibers and fragments ($CSF = 0.25 - 0.75$) with a second peak at a CSF of 0.07, which is mainly attributed to sheets (Kooi and Koelmans, 2019).

CHAPTER 9

RESULTS AND DISCUSSIONS

9.1 MEASURED PARTICLE TRAJECTORIES

Figure 9.7 shows four examples of measured trajectories for experiments 8, 12, 13 and 17. Experiments 8 and 12 have been performed with wave conditions W1 with two different particle size classes, namely with $d_p = 498$ μm and $d_p = 183$ μm, respectively. Similarly, experiments 13 and 17 have been performed with the wave conditions W2, characterized by the same period as W1 but larger wave height, in which another set of particle diameter has been considered ($d_p = 543$ μm and $d_p = 241$ μm, respectively).

It is worth mentioning that for a neutrally buoyant particle, i.e. $\beta = 1$, the expected trajectory driven by the wave Stokes drift would be an open spiral with no net transport in the vertical position after a single wave period (Stokes et al., 1851). As soon as a particle has a density difference with the fluid, i.e. $\beta < 1$, the particle trajectory substantially deviates from the $\beta = 1$ case. Figure 9.7 shows that in each case the particles tend to settle following a trajectories that resemble a spiral that, as time passes, tends to unroll itself. This effect is stronger for larger diameters (Figure 9.7, panels a) and c)). As soon as the settling particle no longer feels the presence of the Stokes drift, the trajectories will be identical to the one expected for pure settling in still fluid, i.e. a straight vertical line. For the smallest diameter (Figure 9.7, panels b) and

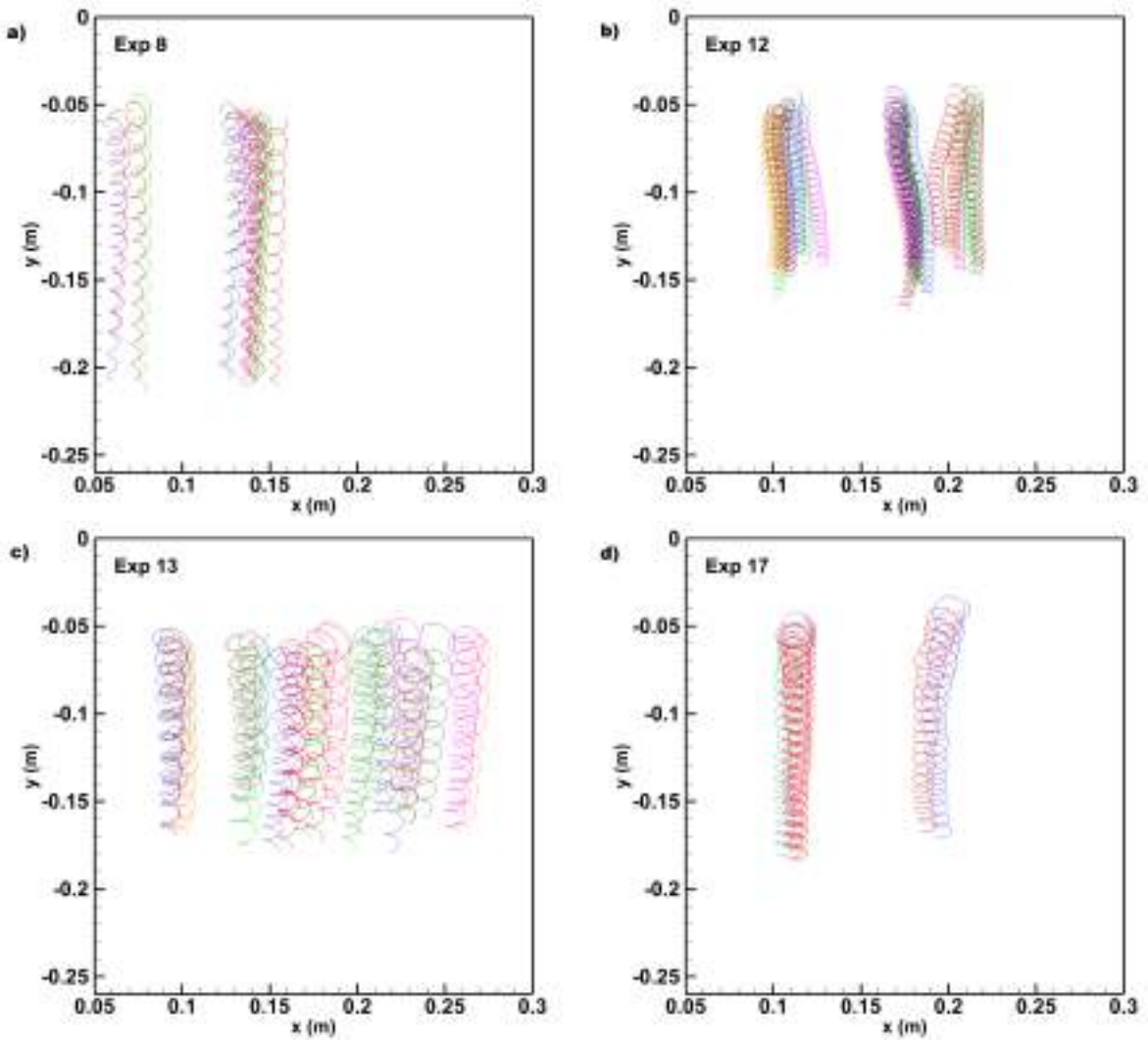

Figure 9.1: Examples of measured trajectories for experiment a) 8, b) 12, c) 13 and d) 17.

d)), the spiral-like trajectories is better preserved during the particle settling, reaching depth comparable with the total flow depth. In all cases, in the limit for long times, the trajectories will be straight vertical lines.

The behavior described above for the experiments reported in Figure 9.7 can be considered typical of all experiments performed during the present study. Similar behaviors have been presented in recent theoretical and numerical studies (Santamaria et al., 2013; DiBenedetto et al., 2018; Stocchino et al., 2019). The inertial character of the particles is the main reason to this difference with respect to the Stokes drift trajectories for a fluid particle. The effect of wave height H translates into a more intense Stokes drift that is felt at greater depths. In fact, the

intensity of the Stokes drift can be estimated from bulk wave parameters (Kumar et al., 2017) and it is proportional to the wave height and the angular frequency. In particular, it depends quadratically on the wave height and linearly on the wave angular frequency. Increasing the wave height H, or equivalently the wave parameter H/gT^2 for a given wave period, will lead the particle trajectories to manifest the rolling character for longer times, experiencing a more intense Stokes drift.

Finally, Figure 9.2 shows the time evolution of the particle velocities for two typical experiments, namely experiment 8 and 12. The interaction between the inertial effects and the Stokes drift leads to an evolution of the velocity components periodic over time, which oscillate with a period equal to the wave period and a decreasing amplitude. Note that the longitudinal velocity component v_x oscillates around a zero value, which will be reached at long time. In fact, as time tends to infinity, the particle reaches a depth where the Stokes drift is no longer acting and, thus, the particle, at that stage, would only settle with a zero horizontal velocity component similarly as still fluid settling. On the other hand, at the long time limit, the vertical velocity reaches an asymptotic value equal to the still fluid settling velocity for that specific particle. Experiments 8 and 12 have been carried out with the same wave conditions and the observed difference highlights the influence of the Stokes number.

9.1.1 The role of the inertial Stokes drift on the net settling velocity

The estimation of the settling velocity of plastic particles in wave-exposed marine environment is of paramount importance for the prediction of plastics dispersion and abundance. The settling velocity enters as physical parameter in several modelling approaches employed to produce large scale prediction of the distribution of microplastics in several sea basins (Isobe et al., 2014; Liubartseva et al., 2016; Zhang and Savenije, 2017; Liubartseva et al., 2018; Jalón-Rojas et al., 2019). So far, the inclusion of the particle settling velocity has been made as a tentative to consider the inertial character of the plastics. In fact, the motion of a spherical inertial particle

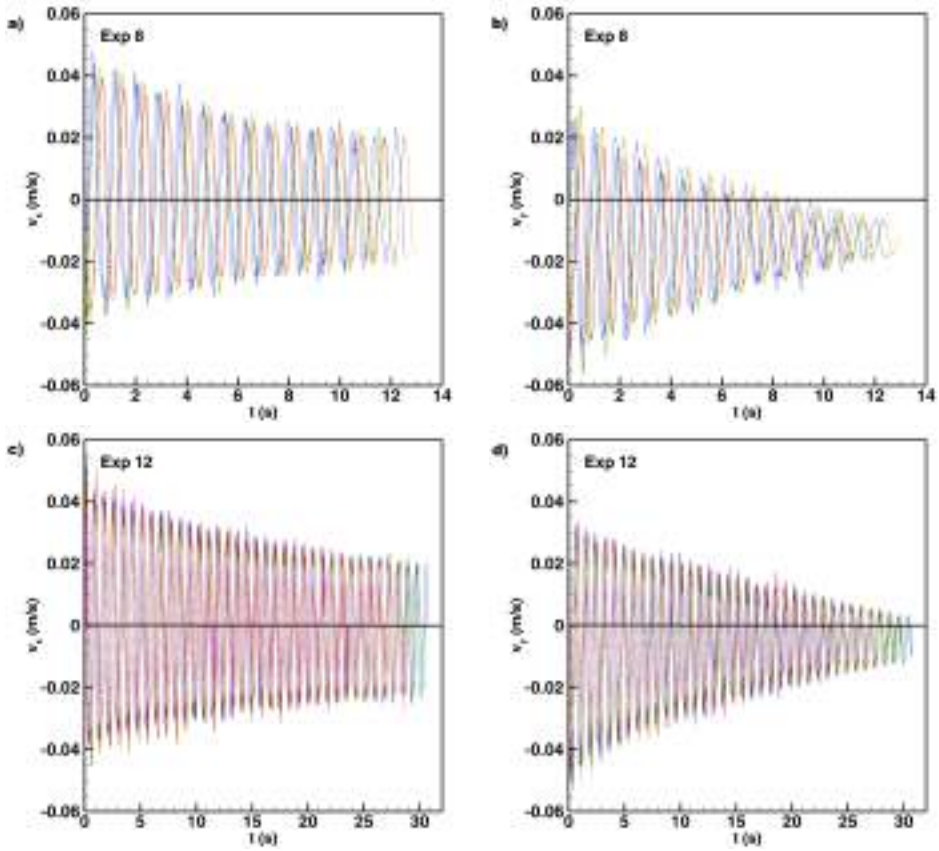

Figure 9.2: Time evolution of the particle velocities: a) experiment 8 x-component, b) experiment 8 y-component, c) experiment 12 x-component and d) experiment 12 y-component

could be described by the following set of equations:

$$\frac{d\mathbf{x}(t)}{dt} = \mathbf{V}(t) \tag{9.1}$$

$$\frac{d\mathbf{V}(t)}{dt} = \frac{\mathbf{u}(\mathbf{x},t)-\mathbf{V}(t)}{\tau} + (1-\beta)\mathbf{g} + \beta\frac{d\mathbf{u}(\mathbf{x},t)}{dt} \tag{9.2}$$

where $\mathbf{V}(t)$ is the Lagrangian particle velocity at the position $\mathbf{x}(t)$ and $\mathbf{u}(\mathbf{x},t)$ the flow field acting on the particle. This model is obtained by the original set of equations of Maxey and Riley (1983) for a spherical particle neglecting the Faxen and Basset terms from the original equations. The solution of the above system provides an accurate description of the physics of the present problem (Santamaria et al., 2013; DiBenedetto et al., 2018; Stocchino et al., 2019) and in more complex oceanographic flows (Beron-Vera et al., 2019). Large scale models for plastic transport, based on Lagrangian and Eulerian equations, often implement the settling velocity as a steady solution of equation (9.2) by equating the drag force term (second term on the right hand side)

and the gravitational force term (third term on the right hand side), disregarding the effect of time dependency of the latter system. Thus, the quest for a good empirical estimator of the settling velocity has inspired numerous studies dedicated to plastic particles (Chubarenko et al., 2016; Khatmullina and Isachenko, 2017; Waldschlager and Schuttrumpf, 2019). The dominant approach was to test the applicability of well-known settling formulas to plastic particles. For instance Khatmullina and Isachenko (2017) used several empirical models developed in other context as settling of natural sediment grains (Dietrich, 1982; Zhiyao et al., 2008) or formulas developed for non-spherical particles (Clift et al., 1978). A recent study followed a similar approach on a wider range of particle parameters (Waldschlager and Schuttrumpf, 2019). However, it should be emphasized that all tested formulas have been developed in pure settling in still fluids, which represent a limiting case since the transport in marine environments are dominated by an intense dynamics and, in particular, by sea waves. Aiming to provide further insight on the settling velocity in wave-exposed environments, the present measurements of particles trajectories obtained for a fairly wide range of particle and wave parameters are further processed to provide estimates of the net settling velocity. In wave context, this latter is defined as the effective settling velocity generated by the effect of the inertial Stoke drift as a result of the interaction between drag forces, described by τ and the gravity force, described by β and wave transport. The analysis is performed on the time evolution of the vertical position $y(t)$ extracted from the full trajectories, see Figure 9.3 for examples where panels a) and c) show the measured trajectories for experiments 8 and 12. The net settling velocity is then directly estimated from the slope of the linear fitting of the $y(t)$ signal (Figures 9.3 b) and d)).

The linear regression filters out the $y(t)$ periodic components with an R-square (R^2) ranging between 0.7 and 0.99, indicating the reliability of the linear model. Figure 9.4 displays the measured net settling velocity in non dimensional form

$$w_s^* = \frac{w_s^3}{g'\nu} \tag{9.3}$$

versus the squared particle Reynolds number

$$R_p^2 = \frac{g' d_p^3}{\nu^2}; \tag{9.4}$$

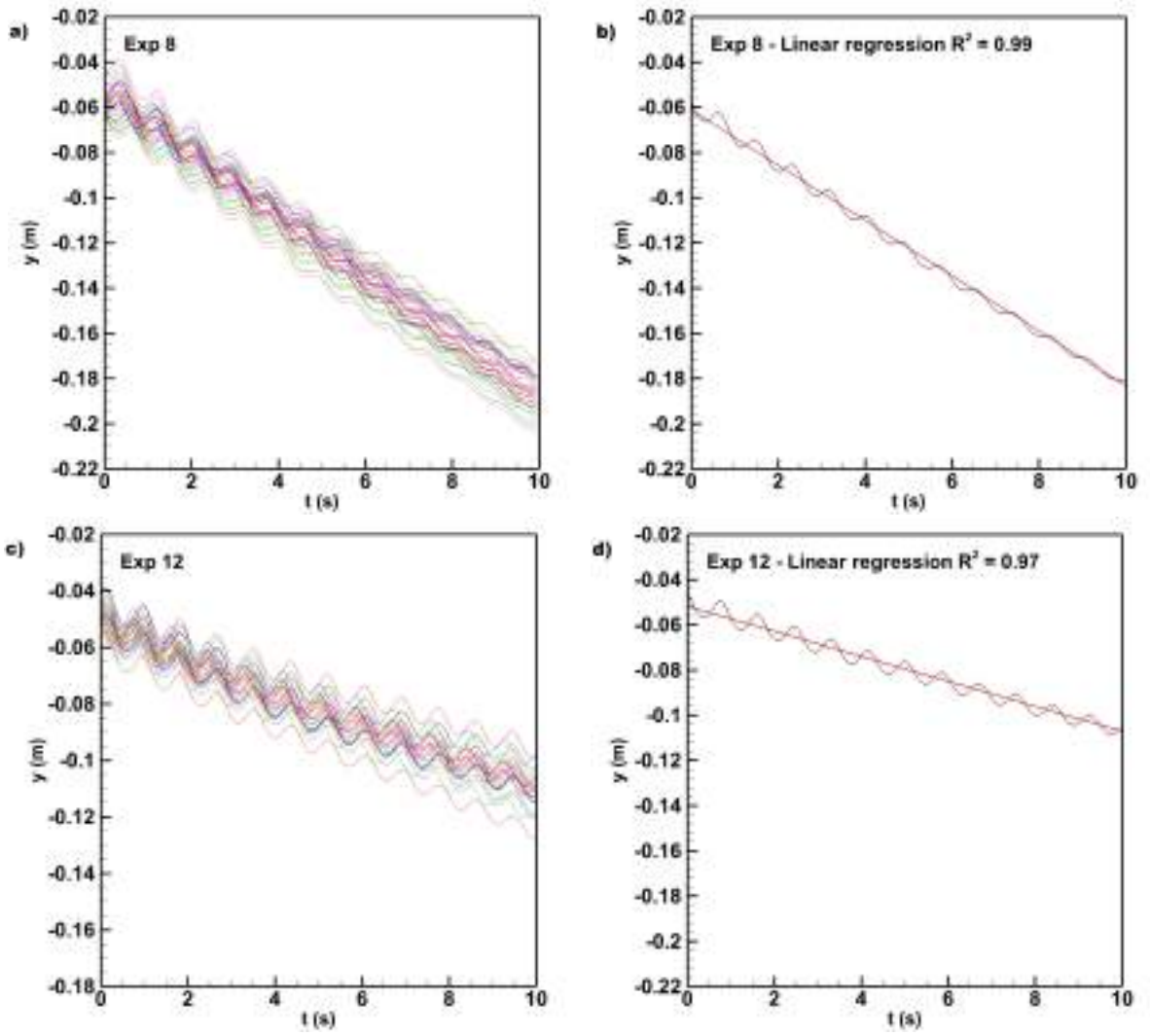

Figure 9.3: Time evolution of the vertical displacements for experiments a) 8 and c) 12. In panel b) and d) are shown the linear regressions of a single track, respectively for experiment 8 and 12.

where $g' = g(\rho_p - \rho_f)/\rho_f$ is the reduced gravity acceleration and ν is the kinematic fluid viscosity (see Khatmullina and Isachenko (2017) for a similar scaling). Note that Figure 9.4 is in loglog coordinates. In the same plot, the theoretical prediction of settling velocity provided by the Dietrich's formula (Dietrich, 1982) is also reported for comparison, as it is commonly used to describe plastics settling velocities. In particular, we have calculated the settling velocity by means of the latter formula for each diameter d_p. As expected the dimensionless settling velocity increases for higher particle Reynolds number. Moreover, it is worth noting that for a fixed value of the particle Reynolds number, R_p, the net settling velocity increases monotonically with the

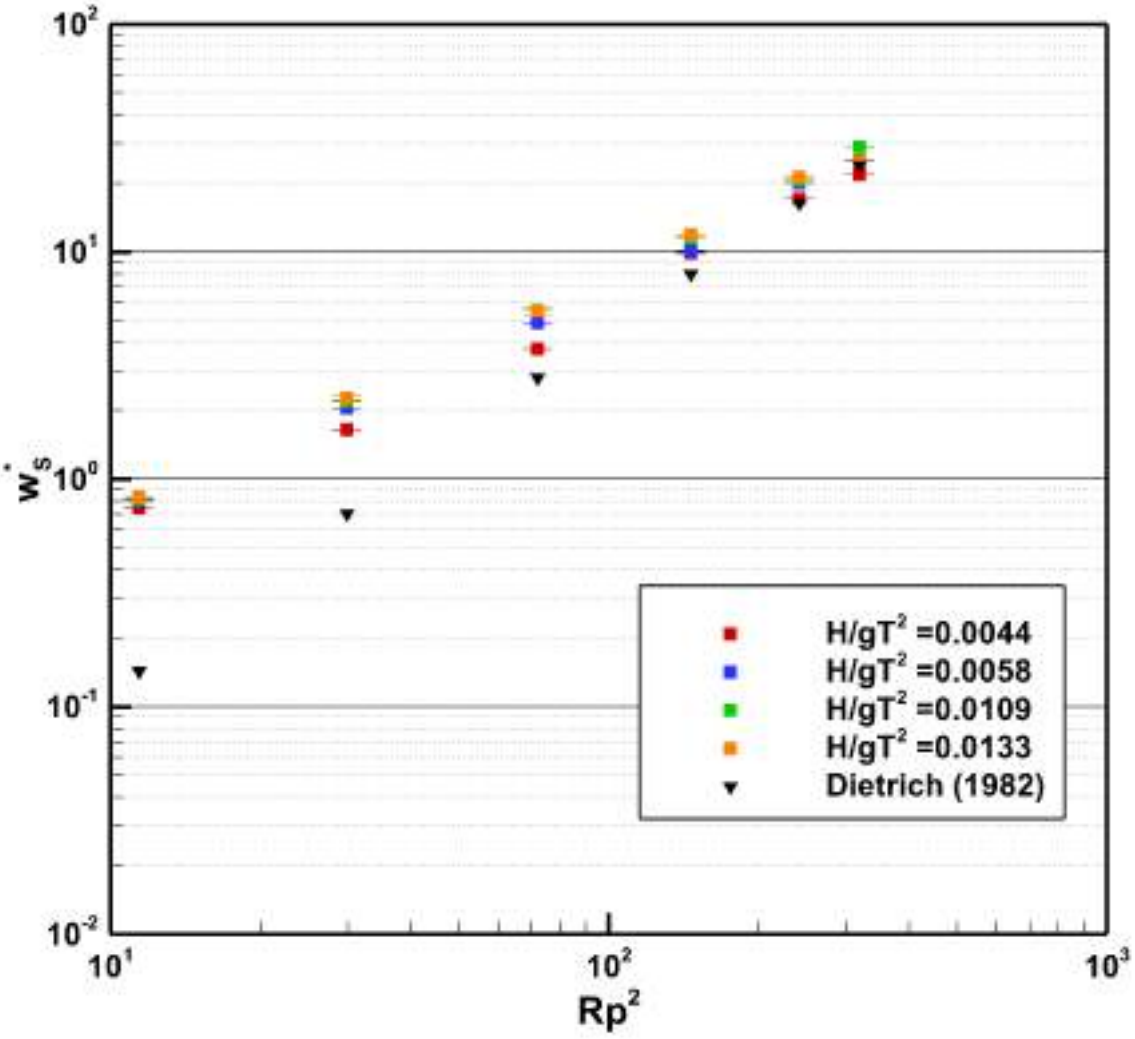

Figure 9.4: Non dimensional net settling velocity w_s^* as a function of the squared particle Reynolds number.

wave parameter, H/gT^2. This observation suggests that increasing the wave amplitude for a given wave period, and therefore increasing the intensity of the Stokes drift, produces an increment of the net settling velocity. Moreover, the effect of the inertial Stokes drift is stronger for small R_p, leading to a greater difference with respect to the still water settling velocity. On the contrary, as R_p increases the particle dynamic tends to a pure settling, collapsing with the settling velocity prediction obtained by Dietrich formula.

To better compare the present results in wave-exposed context with the traditional pure settling velocity formulas, Figure 9.5 depicts the measured net settling velocity w_s^m for all

experiments against the theoretical estimate with the Dietrich formula. The solid line indicates the perfect agreement, whereas the black and blue dashed-dotted lines indicate the ±20% and ±50% thresholds, respectively. The results clearly indicate that the overall effect of the inertial Stokes drift is to increase the settling velocity compared to the case of pure settling in still fluid. Most of the experimental measurements fall inside the region of ±50%. On the contrary, the smallest diameters, which corresponds to the lowest velocities, show the greater differences, indicating that are more sensitive to the effect of the Stokes drift. Santamaria et al. (2013) showed that inertial particles tend to increase the settling velocity under regular waves and only asymptotically tend to the Stokes terminal velocity. Similar results have been obtained numerically with a more refined wave model by Stocchino et al. (2019). The numerical prediction reported in Stocchino et al. (2019) are fairly consistent with the present results. For particle diameters in a range between 300 and 500 μm, the increase with respect to the pure settling velocity was estimated by the numerical simulation of the order of 20% for the smallest diameter and about 6% for the larger. In the present laboratory experiments, for the same diameter, the increase is of the order of 15-20% and 5-9%, respectively.

9.1.2 A NEW FORMULATION OF THE SETTLING VELOCITY

We aim to present an analytic interpretation of the measured settling velocity. As already mentioned, settling velocity formulas are often implemented into numerical models at regional or oceanographic scale and the common choice is to use expression that have been tested in still water (Khatmullina and Isachenko, 2017) and the effect of wave is added using Stokes drift classical formulations. The present laboratory experiments have demonstrated that the interaction of inertial effects and sea wave Lagrangian transport produces a more complex settling dynamics of the plastic particles. Aiming to provide a simple and operable approach, we suggest a new formulation of the settling velocity that empirically takes into account the inertial Stokes drift. The proposed formulation should satisfy the limit when no wave field is acting, i.e. $H/gT^2 = 0$, and thus, the settling occurs as in still water. In this limit case, we have decided to describe the settling velocity by the well established Dietrich formula, which we recall here for the sake of clarity. The Dietriech settling velocity w_s^D can be estimated as:

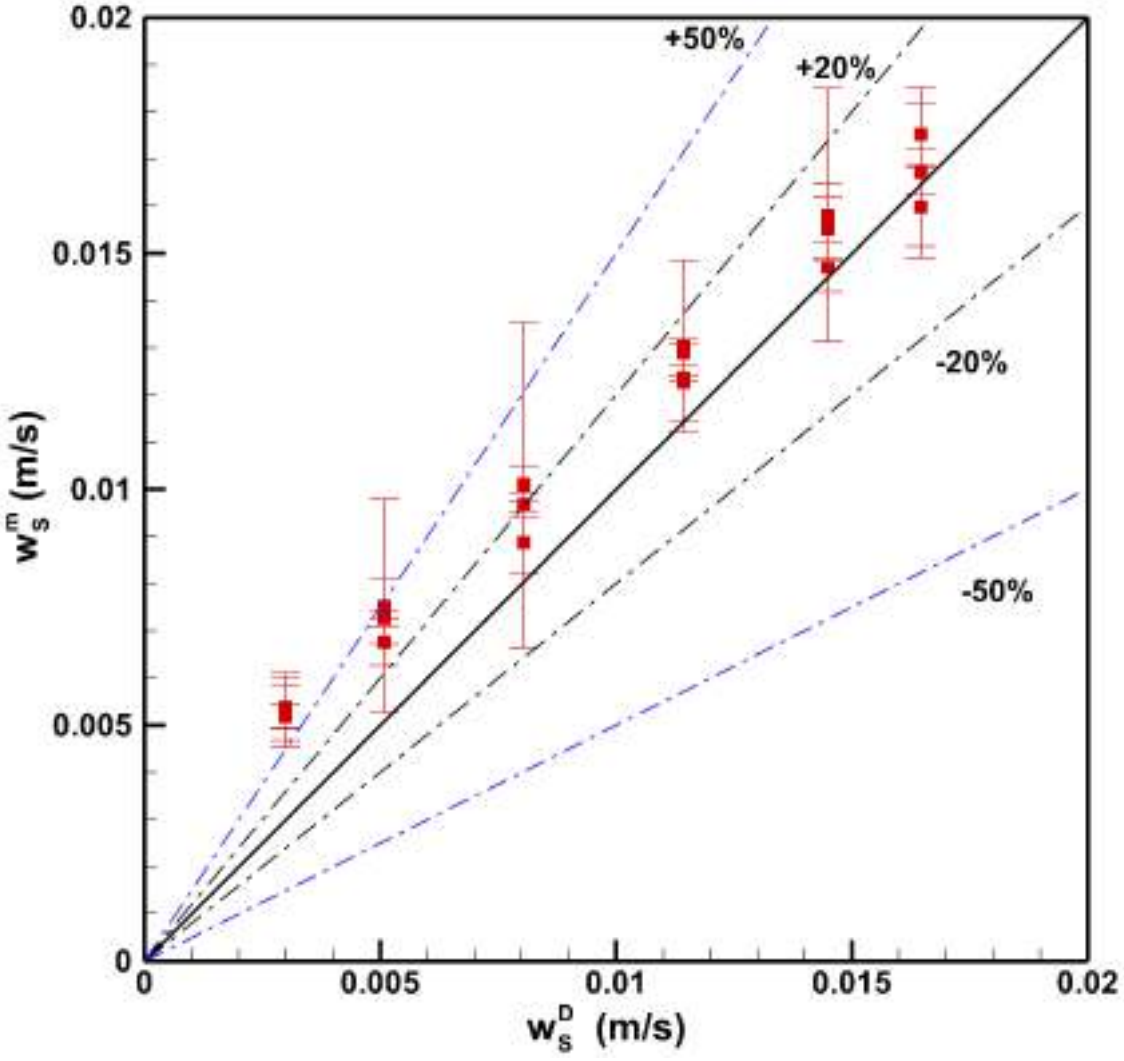

Figure 9.5: Comparison between the measured net settling velocity against the theoretical settling velocity as in Dietrich (1982). Rectangles are the mean of the measured settling velocities with their standard deviation; the black solid line is the plane bisector, indicating perfect agreement, whereas the black and the blue dot dashed line represent the ±20% and ±50% intervals of confidence respectively.

$$w_s^D = \sqrt{\frac{g'}{g} d_P} R_f \tag{9.5}$$

where R_f is:

$$\begin{aligned} R_f = \exp\{ & -b_0 + b_1 \ln(R_P) - b_2 [\ln(R_P)]^2 \\ & - b_3 [\ln(R_P)]^3 + b_4 [\ln(R_P)]^4 \} \end{aligned} \tag{9.6}$$

in which the coefficient were fitted on experimental data and assume the values:

- b_0 = 2.89139,
- b_1 = 0.95296,
- b_2 = 0.05683,
- b_3 = 0.00289,
- b_4 = 0.00024.

Note that the original values of the coefficient have been change in order to implement the natural logarithm instead of the base-10 logarithm as in the original form (Dietrich, 1982).

Starting from the measured non-dimensional settling velocity defined as the ratio between the experimental net settling velocity w_s^m and the velocity w_s^D provided by equation (9.5), we intend to represent the dependency on the main parameters, namely the particle Reynolds number R_p and the wave parameter H/gT^2, using the following formulation:

$$\frac{w_s^m}{w_s^D} = 1 + a R_P^b \left(\frac{H}{gT^2} \right)^c \tag{9.7}$$

where the coefficients a, b and c are evaluated as the best fit on the experimental data. A non-linear surface fitting is applied, based on an iterative *Trust-Region-Reflective Least Squares* algorithm (Moré and Sorensen, 1983; Steihaug, 1983; Coleman and Li, 1996). Applying this procedure on the experimental data, using equation (9.7), leads to the values of the parameters

$a = 97$, $b = 8/5$ and $c = 3/5$. The fitted surface is shown in Figure 9.6 together with the experimental data. The goodness of the non-linear fitting is quantified using several statistical metrics, in particular the Sum of Squares Due to Error (SSE), R-Square (R^2) and the Root Mean Squared Error ($RMSE$). For the present database, we obtained $SSE = 0.1798$, $R^2 = 0.9108$ and $RMSE = 0.0787$. The small values of SSE and $RMSE$ indicate that the model used to describe the dataset through equation (9.7) shows a small random error component, implying that the model is robust in terms of prediction in the parameter space. Moreover, the high value of the R^2 indicates that the suggested formula describe about the 91% of the total variation in the data about the average. The overall goodness of fitting values confirms that the proposed model is statistically robust in representing the experimental observations and gives confidence for a more general application on the estimation of settling velocity of microplastics particles exposed to wave action.

9.1.3 SCALING ARGUMENT AND APPLICABILITY OF THE RESULTS.

The present results have been obtained using a laboratory wave flume as described in the methods section. It is worth discussing the limitation and applicability of the measurements, comparing the set up and controlling parameters with the actual field observations. Scale reproduction of free surface flows, such as waves, is typically achieved through a partial similarity of Froude number, defined as in equation (8.10). As a consequence of this choice, some of the parameters used for the present analysis require a proper scaling in order to extend the results at real world conditions. Froude similitude implies that a geometrical reduction scale λ should be associated with a time scale reduction as $\lambda^{1/2}$, which also ensures the preservation of the wave parameter H/gT^2 between the model and the real sea waves. The present laboratory waves in the range of $H/gT^2 = 0.004 - 0.013$ are representative of realistic sea state conditions, see Stocchino et al. (2019) for comparison. The main particle parameters that have been used in the present study are the Stokes number S_t and the particle Reynolds number R_p. In Froude similitude, both are scaled as a typical Reynolds number and, thus, as $\lambda^{3/2}$. The range of the parameters investigated at laboratory scale are $S_t = 0.023 - 0.363$ and $R_P = 3.39 - 17.9$ for a fixed value of the particle density that correspond to $\beta = 0.8876$. The direct comparison of such ranges at field scale is not straightforward due to the fact that, despite the great amount of literature reporting field

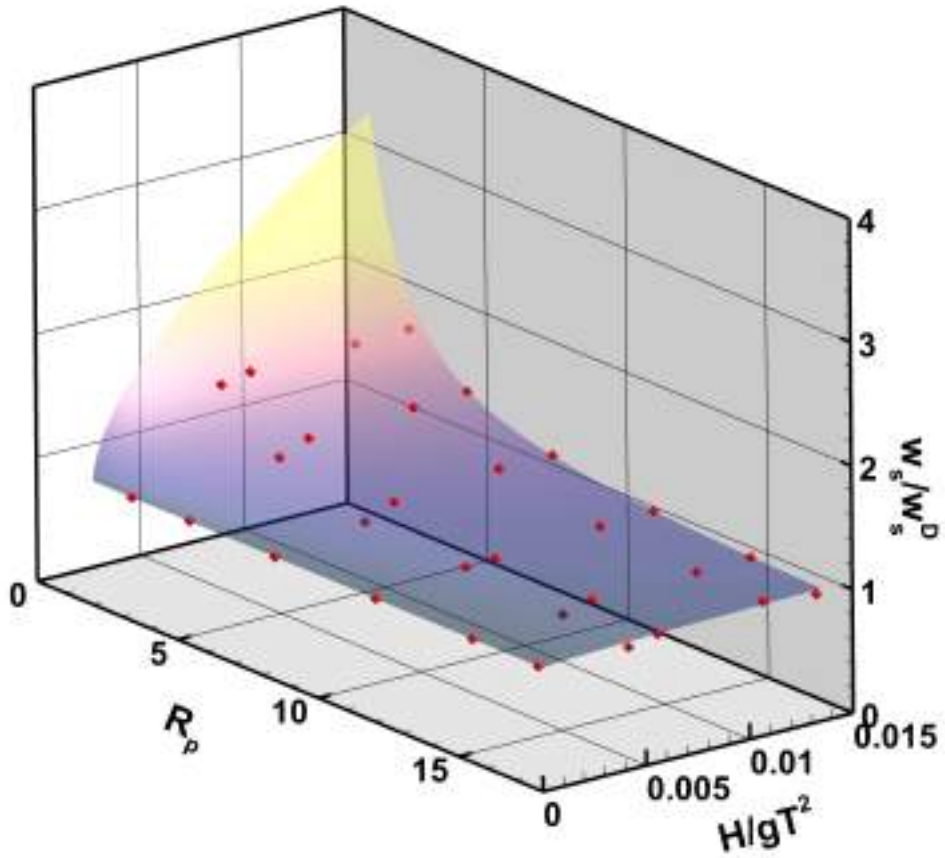

Figure 9.6: Reconstructed surface using equation (9.7) in the parameter space (R_p, H/gT^2) versus the experimental net settling velocity.

observations of plastic debris in different sea/ocean basins and different compartments (water surface, water column and sediment), it remains difficult to have a comprehensive information on particle size and density. Hidalgo-Ruz et al. (2012) presented an interesting review based on 68 studies trying to summarize the range of particle debris in terms of sizes and densities. However, it is interesting to note that heavy particles have been often collected during sediment sampling with quite a wide range of sizes (McDermid and McMullen, 2004; Morét-Ferguson et al., 2010). We base our estimate of the Stokes number and particle Reynolds number on a recent work (Kooi and Koelmans, 2019) where an helpful statistical interpretation of the data derived from eleven published studies is presented. In particular a multidimensional probability density functions (pdf) involving size, density and shapes of the debris has been proposed. In particular,

the distribution of plastic density is well fitted by a Normal-Inverse Gaussian distribution with a central value of around 1000 $kg.m^{-3}$ and a marked positive skewness with non negligible probability values up to 1600 $kg.m^{-3}$ (Kooi and Koelmans, 2019). From this analysis about 45% of the observed plastic debris have a density in a range between 960 and 1580 $kg.m^{-3}$, not considering the chemical and weathering process that tend to increase plastic density, see table S3 of Kooi and Koelmans (2019). Based on the analysis of Kooi and Koelmans (2019), in particular the data of their Figures S1 and S4 and Table S3, we used a range of particle size $d_p = 100 - 4000\mu$m and density $\rho_P = 1030 - 1300\ kg.m^{-3}$. Using a range of wave parameter similar to the one used for the present experiments, the Stokes number and the particle Reynolds number obtained are $S_t = 0.002 - 11$ and $R_P = 0.5 - 430$ for a range of added-mass parameters β between 0.848 and 0.997. The experimental ranges of S_t and R_P are therefore fully included in the ranges expected at field scale. We could conclude that the present formulation for a net settling velocity of heavy particles well represent the realistic conditions of the transport of plastic particles by sea waves, for quite a wide range of realistic plastic characteristics. We acknowledge the limitation of the present study in considering only spherical particles and the fact that our wave flume does not allow for the generation of sea wave in deep water conditions. The former issue will deserve further investigations based on the present study. The latter, however, it is not considered as a main factor in the dynamics of negatively buoyant particles.

9.2 Numerical Particle trajectories, velocities and accelerations

Particles trajectories were computed using the system (8.11), and typical examples for a fixed Stokes number ($S_t = 2 \times 10^{-3}$) are shown in Figure 9.7 for two waves conditions, $H/gT^2 = 0.001$ and $H/gT^2 = 0.006$, and varying the values of the random term in the equations.

For very low value of the coefficient D (panels a) and d)), the particle trajectories are similar to the one computed in previous studies (Santamaria et al., 2013; Stocchino et al., 2019) or measured in the laboratory experiments of section 9.1 and seen in De Leo et al. (2021). The inertial character of heavy particles, already at low value of the Stokes number, interacts with the wave Stokes drift leading to an augmented settling velocity. The net settling velocity was experimentally measured and was found to depend on both the particle characteristics and the

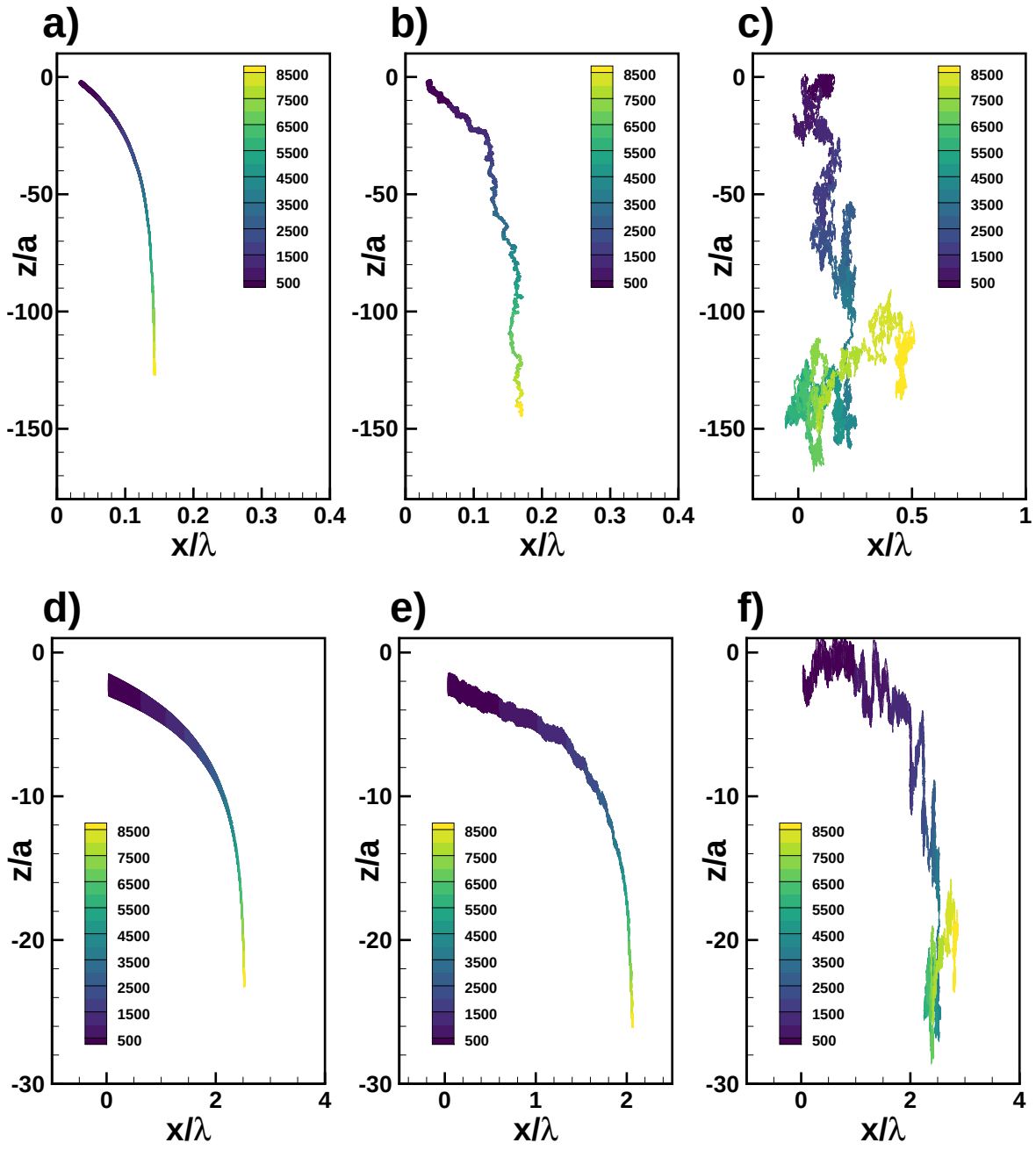

Figure 9.7: Example of particle trajectories for the same particle, $S_t = 2 \times 10^{-3}$, and different waves and coefficient D. $H/gT^2 = 0.001$: a) $D = 10^{-6}\mathrm{m}^2\mathrm{s}^{-1}$; b) $D = 10^{-3}\mathrm{m}^2\mathrm{s}^{-1}$; c) $D = 10^{-1}\mathrm{m}^2\mathrm{s}^{-1}$. $H/gT^2 = 0.006$ d) $D = 10^{-6}\mathrm{m}^2\mathrm{s}^{-1}$; e) $D = 10^{-3}\mathrm{m}^2\mathrm{s}^{-1}$; f) $D = 10^{-1}\mathrm{m}^2\mathrm{s}^{-1}$. For all panels particle has been released in the same position and at the same time. The colors represent the time.

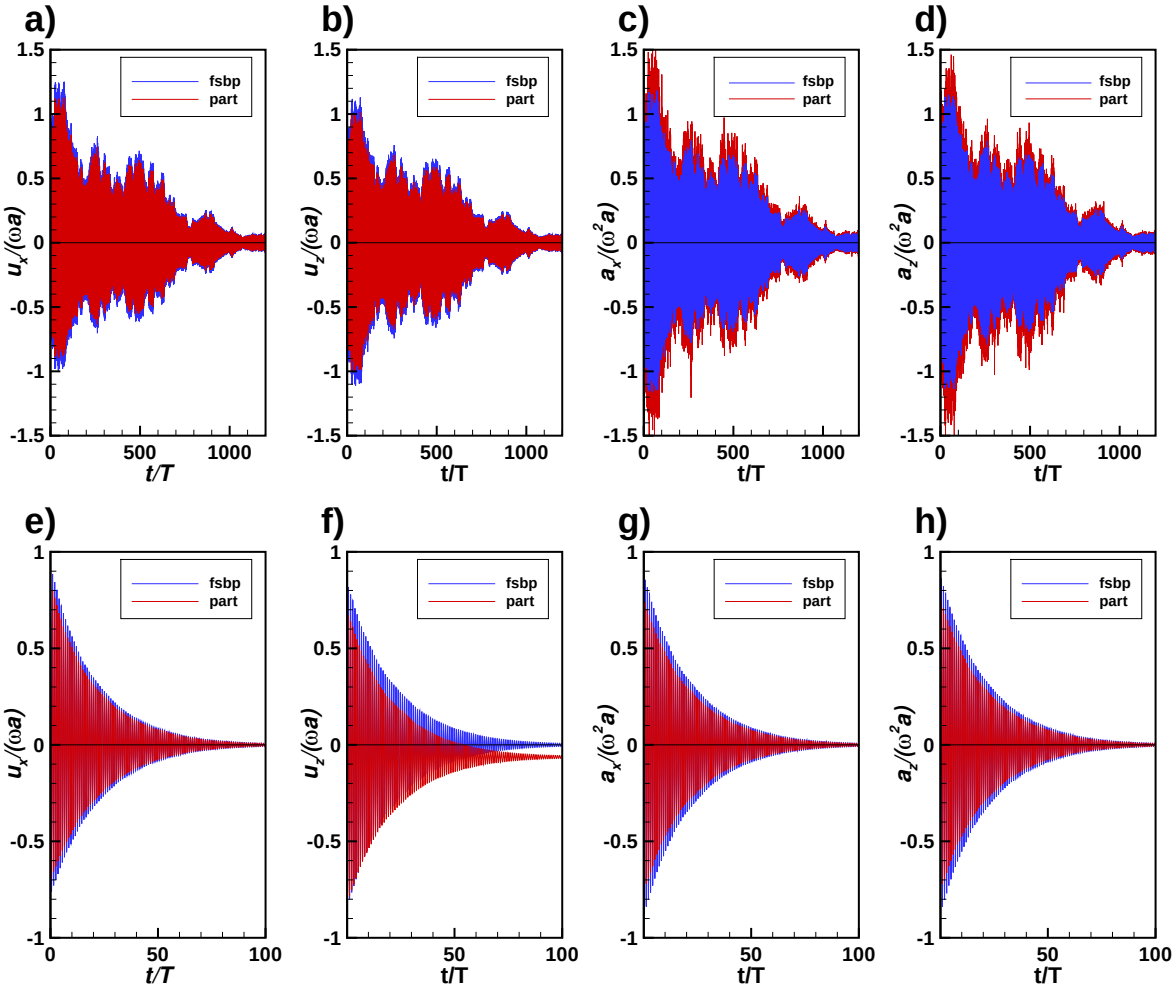

Figure 9.8: Example of non dimensional velocities and accelerations time signals for two values of the Stokes number and for the same wave parameter ($H/gT^2 = 0.006$) and diffusion coefficient ($D = 10^{-3}\mathrm{m}^2\mathrm{s}^{-1}$). Panels a) - d) $S_t = 9 \times 10^{-4}$, panels e) - h) $S_t = 5.77 \times 10^{-2}$.

wave parameter (De Leo et al., 2021).

Following the theoretical predictions of Santamaria et al. (2013) under linear waves approximation, the maximum dimensionless longitudinal distance traveled by the particle owing the sea waves depends on the added-mass parameter β, the wave Froude number and the Stokes number. As shown in Figure 9.7, the maximum distance in the wave propagation is several wavelengths. Increasing the value of the background random process through the coefficient D leads to, as expected, less regular trajectories, see panels b), c), e) and f). Note that Figure 9.7 shows only one particle trajectory out of the 3500 particles used.

For the present purpose, the velocities and accelerations time signals of the particle and the *fluid seen by particle* (Pozorski and Minier, 1998, 1999; HE et al., 2006; Jung et al., 2008) were also calculated. Examples of the computed non dimensional longitudinal and vertical velocities $(u_x/(\omega a), u_z/(\omega a))$ and accelerations $(a_x/(\omega^2 a), a_z/(\omega^2 a))$ are shown in Figure 9.8 for the most intense wave conditions and two different values of the Stokes number, panels a) - d) $S_t = 9 \times 10^{-4}$ and panels e) - h) $S_t = 5.77 \times 10^{-2}$. In all cases the coefficient D was set at $10^{-6}\mathrm{m}^2\mathrm{s}^{-1}$. Note that particle variables are drawn in red and *fluid seen by particle* variables in blue.

In all cases, velocities and accelerations tend to decrease oscillating around an asymptotic value. The asymptotic values of the longitudinal velocities and both components of the acceleration tend to zero, as soon as the particles reach a depth where the wave velocity field is no longer felt. The depth at which the wave velocities are zero depends only on the wave parameter, whereas the time at which the particles reach this depth depends on the particle properties. At this depth, heavy particles tend to behave as settling particles in still fluid, thus, their vertical velocity is simply described by the Stokes settling velocity (Santamaria et al., 2013)

$$w_s = -(1-\beta)g\tau. \tag{9.8}$$

It is worth noting that the vertical velocity of the *fluid seen by particle* tends to zero differently from the particle vertical velocity. This is clearly visible in panel f), where the vertical velocity of the heavy particle tends to a constant non zero value (the Stokes settling velocity). Moreover, the random contribution $\sqrt{2D}\mathbf{R}(t)$ modifies the velocities and acceleration at the small Stokes number, see Figure 9.8 panels a) - d), whereas it is already ineffective for Stokes number of order 10^{-2}, see panels e) - f). For larger Stokes number, the effect of the stochastic terms is even less important also for the highest value of the coefficient D.

9.2.1 Lagrangian auto-correlation functions and Integral Scales

9.2.1.1 Definition of the auto-correlation functions

tarting from the trajectories computed using the system (8.11), we first introduce the Lagrangian auto-correlation functions and, then, we discuss their shapes and integral time scales depending

on the main controlling parameters. The knowledge of their shapes is essential to understand the dispersion process (Boi et al., 2018).

For a generic variable g, we define the Lagrangian auto-correlation function as:

$$\rho_g(\tau) = \langle g(t)g(t+\tau)\rangle \tag{9.9}$$

where the brackets indicates an ensemble average. Considering, at this moment, the fluid velocities (u_x, u_z) and fluid acceleration (a_x, a_z), we can define the normalized Lagrangian auto-correlation function as:

$$\begin{aligned} \mathscr{R}_{u_x}(\tau) &= \frac{\rho_{u_x}(\tau)}{\sqrt{\rho_{u_x}(0)^2}}, \qquad \mathscr{R}_{u_z}(\tau) = \frac{\rho_{u_z}(\tau)}{\sqrt{\rho_{u_z}(0)^2}}, \\ \mathscr{R}_{a_x}(\tau) &= \frac{\rho_{a_x}(\tau)}{\sqrt{\rho_{a_x}(0)^2}}, \qquad \mathscr{R}_{a_z}(\tau) = \frac{\rho_{a_z}(\tau)}{\sqrt{\rho_{a_z}(0)^2}}. \end{aligned} \tag{9.10}$$

The auto-correlations are then used to evaluate the Lagrangian integral scales T_u as:

$$\begin{aligned} T_{u_x} &= \int_0^{+\infty} \mathscr{R}_{u_x} d\tau, \qquad T_{u_z} = \int_0^{+\infty} \mathscr{R}_{u_z} d\tau, \qquad T_u = \frac{1}{2}(T_{u_x} + T_{u_z}), \\ T_{a_x} &= \int_0^{+\infty} \mathscr{R}_{a_x} d\tau, \qquad T_{a_z} = \int_0^{+\infty} \mathscr{R}_{a_z} d\tau, \qquad T_a = \frac{1}{2}(T_{a_x} + T_{a_z}). \end{aligned} \tag{9.11}$$

Similarly we can define the normalized auto-correlation functions and their corresponding integral scales for the particle velocities and accelerations (indicated in the following with a superscript p) and the *fluid seen by particle* velocities and acceleration (indicated in the following with a superscript f).

In general, the normalized auto-correlation functions of the fluid, the particle and the *fluid seen by particle* could display a different behavior; note that in case of a passive tracer (limiting case for mass-less particle) all these quantities collapse together and are equal to the ones calculated for the carrier fluid.

Following the Taylor's theory (Taylor, 1921), formulated for tracers, or its recent generalization to different dynamical models for inertial particles (Boi et al., 2018), the definition of a diffusion coefficient is inherently related to the finite value of the limit time that tends to infinity of the auto-correlation functions. Thus, a time independent diffusion coefficient requires that the auto-correlation functions decay rapidly in time, regardless if we are considering tracers or inertial particles.

Commonly, the velocity fields used to compute the auto-correlations functions and integral scales are built removing an average component when present. In the present case, no background constant flow is added to the wave field. However, care must be taken when the vertical velocity is considered. In fact, when the particles reach a certain depth, the leading order term in the particle velocity equation, see (8.11), is the buoyancy term, (Santamaria et al., 2013). This term, being independent of time, would produce a spurious effect on the auto-correlation function and, ultimately, a long-time mean-square dispersion that grows as time squared. Thus, the $\mathscr{R}^p_{u_z}$ has been evaluated subtracting the asymptotic settling velocity reached by the particle when the effects of wave fields are no longer felt, namely $u_z^{'} = u_z - w_s$, where w_s is the Stokes settling velocity.

The integral Lagrangian scales defined above can be considered as an *internal* time scales determined by the dynamic described by the system (8.11), provided the Eulerian velocity field computed with the system (8.4). In the problem at hand, however, other *external* time scales appear, namely the wave period T (typical of the fluid flow) and the Stokes time τ (typical of the particle).

The wave periodicity is of particular interest; in fact, the periodicity of the velocity wave field and the resulting Stokes drift is felt also by the particle motion, see Figures 9.7 and 9.8, and its derived properties. The looping character of the particle position and velocity is reflected on a looping-like auto-correlation function. The wave period is the external time scale related to the flow forcing and, not surprisingly, it is reflected in the auto-correlation that assumes a looping shape, whereas this tends to zero (Farazmand and Sapsis, 2019).

9.2.1.2 Velocity and acceleration auto-correlation functions of inertial particles and *fluid seen by particles*

Figure 9.9 shows the particle horizontal and vertical velocity auto-correlations for the test 000 ($H/gT^2 = 0.001$), and for several Stokes numbers and the extreme values of D, namely 10^{-6} $\mathrm{m^2 s^{-1}}$, panels a) and b), and 10^{-1} $\mathrm{m^2 s^{-1}}$, panels c) and d).

Although both $\mathscr{R}^p_{u_x}$ and $\mathscr{R}^p_{u_z}$ tend to zero as time grows, they oscillate around the zero value as shown in the box in panel b). Comparing panel a) with b) and panel c) with d) there are no

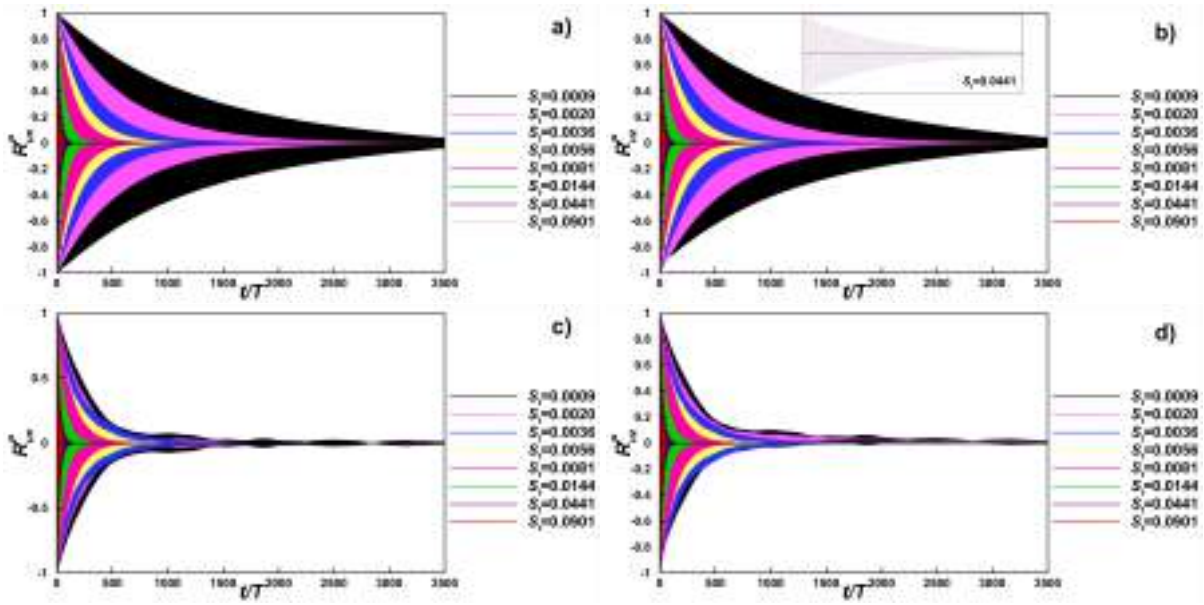

Figure 9.9: Normalized velocity auto-correlation for the experiment with $H/gT^2 = 0.001$: a) $\mathscr{R}^p_{u_x}$ with $D = 10^{-6}\mathrm{m}^2\mathrm{s}^{-1}$, b) $\mathscr{R}^p_{u_z}$ with $D = 10^{-6}\mathrm{m}^2\mathrm{s}^{-1}$, c) $\mathscr{R}^p_{u_x}$ with $D = 10^{-1}\mathrm{m}^2\mathrm{s}^{-1}$; d) $\mathscr{R}^f_{u_z}$ with $D = 10^{-1}\mathrm{m}^2\mathrm{s}^{-1}$. In panel b) a zoom in is also inserted to show clearly the looping character of the auto-correlation functions.

substantial differences between the auto-correlation of the two velocity components. However, we will see in the following that the integral scales show a more marked anisotropy.

Increasing the coefficient D leads to two main effects, see panels c) and d): the envelope of the auto-correlation functions tends to zero in shorter times and low frequency oscillations appear. These effects are more clearly visible for low Stokes numbers, whereas higher Stokes number are less sensitive to the Gaussian noise. The appearance of low frequency loops is even more evident with increasing the wave parameter, e.g. for test 003 where the wave parameter has the highest value of the present study ($H/gT^2 = 0.006$), see Figure 9.10.

Three values of the Stokes number are reported for the lowest and highest value of the coefficient D. For the case with $S_t = 0.002$, panels a) and b), and the case with $S_t = 0.0036$, panels c) and d), the vertical auto-correlation shows low frequency loops even with the lowest values of the turbulent diffusion coefficient, whereas for $D = 10^{-1}\mathrm{m}^2\mathrm{s}^{-1}$ these lobes are more frequent (panels b) and d)).

Differently from previous studies where the vertical velocity auto-correlation increases, reaching almost a constant shape either in the absence of gravity effects (Jung et al., 2008; Wetchagarun

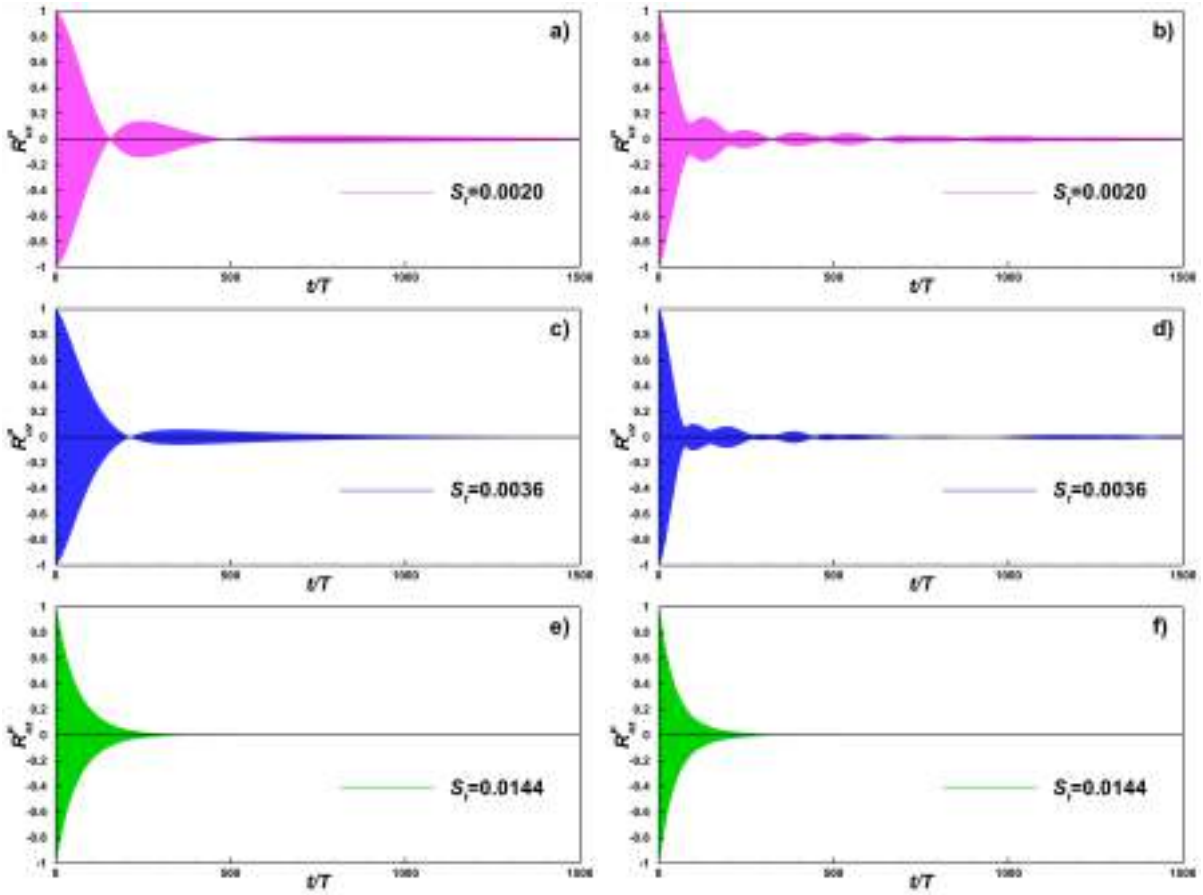

Figure 9.10: Normalized vertical velocity auto-correlation $\mathscr{R}^p_{u_z}$ for the experiment with $H/gT^2 = 0.006$ with two values of the coefficient D, namely $D = 10^{-6}\mathrm{m}^2\mathrm{s}^{-1}$ panels a), c) and e), and $D = 10^{-1}\mathrm{m}^2\mathrm{s}^{-1}$ panels b), d) and f), for three values of the Stokes number.

and Riley, 2010) or when gravity is considered (Wang and Stock, 1993), we found that increasing the Stokes number produces oscillating auto-correlation functions with envelopes that tend to decrease more rapidly to zero. However, the latter aspect will turn out to be misleading in the computation of the integral scales, as discussed in the next section.

Moreover, negative loops are reported by Wang and Stock (1993) only in the longitudinal correlation for low or intermediate values of their drift parameters, a measure of the gravity effects compared to the fluid velocity variance. On the contrary, the vertical correlation calculated by Wang and Stock (1993) has a monotonic time decay and increasing values with S_t.

In the present case, the looping character of the auto-correlations does not disappear for increasing Stokes number for both directions, $\mathscr{R}^p_{u_x}$ and $\mathscr{R}^p_{u_z}$. Regarding the looping character of

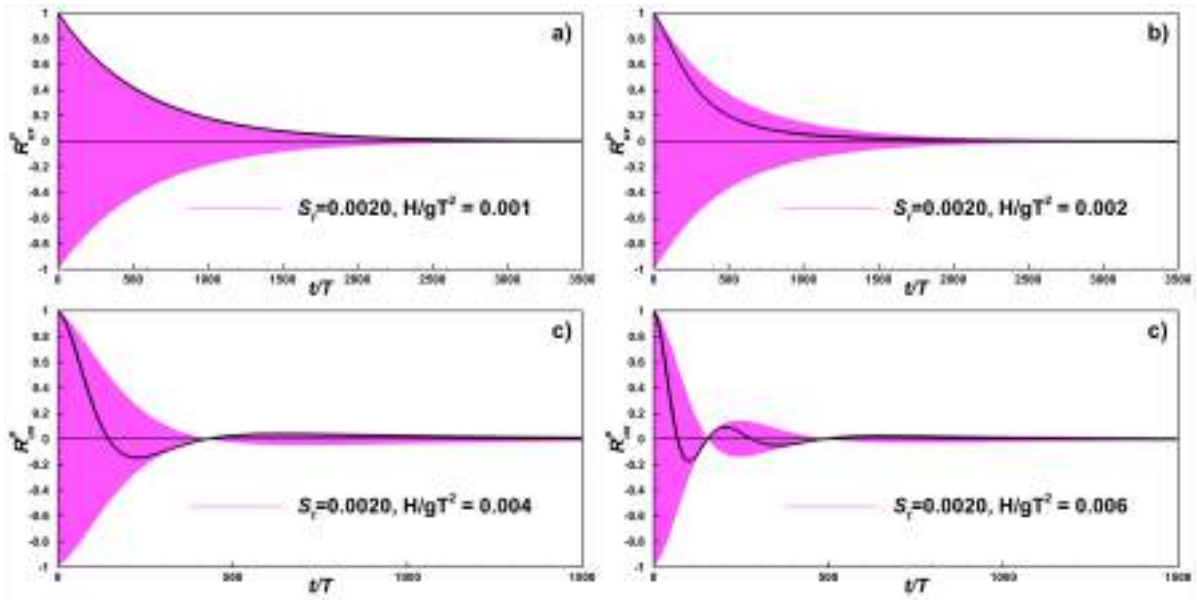

Figure 9.11: Normalized horizontal velocity auto-correlation $\mathscr{R}^p_{u_x}$ for all wave conditions, same coefficient $D = 10^{-6}\mathrm{m}^2\mathrm{s}^{-1}$ and Stokes number equal to 0.002. Black lines indicate the auto-correlations sampled every period.

the auto-correlations, it is interesting to note that the oscillations of the auto-correlation functions occur with a periodicity that does not always coincide with the wave period. Figure 9.11 shows the cases for the same Stokes number ($S_t = 0.002$) and diffusion coefficient ($D = 10^{-6}\mathrm{m}^2\mathrm{s}^{-1}$) for the different wave conditions. In the Figure, the $\mathscr{R}^p_{u_x}$ is reported for every instant together with its wave-period sampled value (black line).

For low wave parameter, panel a), the envelope of the auto-correlation functions coincides with its period-sampled values. Increasing the wave parameter H/gT^2, from panel b) to d), the difference between the envelope of the auto-correlation function and its period-sampled value is increasingly noticeable. The non-linear interaction between the typical time scale of the flow and the particle time scales leads to the generation of oscillations with frequency slower then the forcing wave period. Similar behavior is found for the vertical velocity auto-correlation functions. If now we compare the correlations of the inertial particles with the *fluid seen by particles*, in all cases the shapes of the auto-correlation functions are extremely similar, whereas we will see that differences are detected in their integral scales.

Finally, no substantial differences in terms of shapes are detected when the acceleration auto-

correlation functions are computed.

9.2.1.3 The dependency of the Lagrangian integral time scales on the particle and flow parameters

We now analyze the Lagrangian integral time scales. The complex shapes of the auto-correlation functions and their dependence on S_t and H/gT^2 is reflected on the variability of the integral scales.

Figure 9.12 summarizes the main findings for the velocity integral scales T_u^p and T_u^f and for the acceleration integral scales T_a^p and T_a^f. Note that the values are normalized with the velocity and acceleration integral scales of the fluid, which assumes values of the order of the wave period T. The different plots correspond to the four values of H/gT^2 and to the two extreme values of the turbulent diffusion, namely $D = 10^{-6}$ and $10^{-1}\mathrm{m}^2\mathrm{s}^{-1}$. Regarding the velocity integral scales of the particle (T_u^p) and of the *fluid seen by particles* (T_u^f), panels a) and c), both tend to monotonically decrease for increasing Stokes where $S_t < 10^{-1}$, whereas their trends seem to change for larger values, possibly, indicating an increase for Stokes number that tends to 1.

The effect of the different wave parameters H/gT^2 is again visible for S_t greater than 10^{-1}. In fact, increasing H/gT^2 leads to a more intense wave Stokes drift, owing to its quadratic dependence on the wave height (DiBenedetto et al., 2018), and, thus, to a more intense convective transport. The values of T_u^p and T_u^f remain lower than the integral scale of the fluid (i.e. $(T_u^p, T_u^f)/T_u << 1$) for the entire range of Stokes number and wave parameters investigated.

Wang and Stock (1993) found similar behaviors, in fact, for low S_t the crossing trajectory effects are dominant and yields shorter particle time scales, whereas inertia makes $T_u^p > T_u$ already for $\mathcal{O}(S_t) \sim 1$. In the present case, we did not investigate the regime where $S_t \geq 1$, where we expect the buoyancy terms of system (8.11) to be dominant and lead to a process close to the standard settling process in still fluid.

As far as the integral velocity time scale for the *fluid seen by particles* T_u^f is concerned, it follows closely the particle counterpart for S_t less than 0.1, especially for high values of the wave parameter. For weak wave $H/gT^2 = 0.001, 0.002$, T_u^f deviates from the particle velocity integral scales and tends to have a non monotonic dependence on Stokes, with a minimum value around

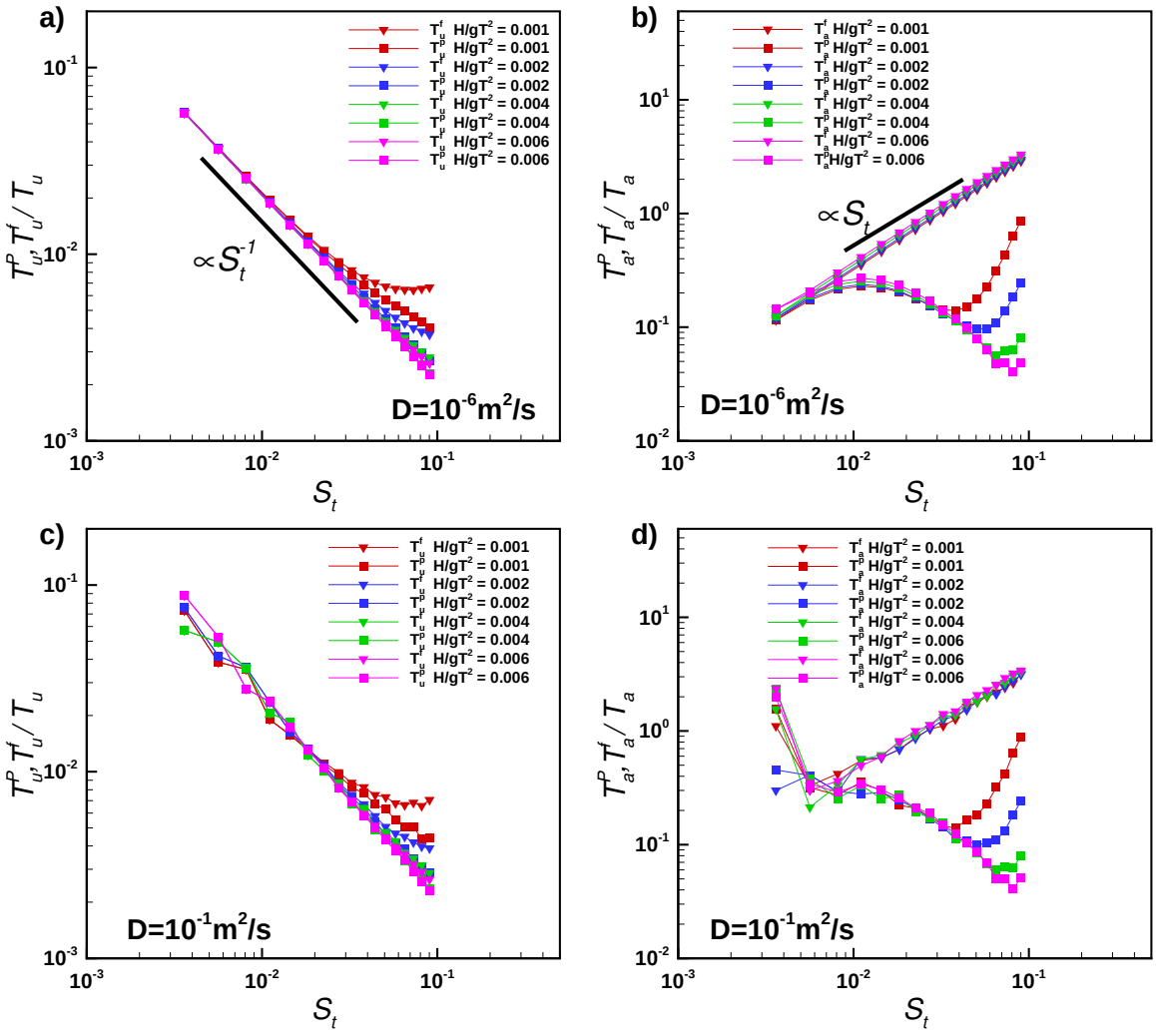

Figure 9.12: Normalized integral time scales as a function of S_t for all experiments and for two values of D: a) velocity integral time scale for $D = 10^{-6}\mathrm{m}^2\mathrm{s}^{-1}$; b) acceleration integral time scale for $D = 10^{-6}\mathrm{m}^2\mathrm{s}^{-1}$; c) velocity integral time scale for $D = 10^{-1}\mathrm{m}^2\mathrm{s}^{-1}$; b) acceleration integral time scale for $D = 10^{-1}\mathrm{m}^2\mathrm{s}^{-1}$. Square symbols indicate the particle times and the delta symbols the *fluid seen by particle* times.

$S_t = 0.25$.

For higher values of the wave parameter, it is reasonably to assume that the higher is the convective velocity (fluid Stokes drift), the closer the particle and its fluid counterparts behave. Moreover, in a wide range of Stokes number, the integral velocity scales show a negative power law fitting in the Stokes number of the kind $T_u^p, T_u^f \propto S_t^{-1}$ ($R^2 = 0.99$), see panel a). The range of validity of the power law increases with higher wave parameters.

The influence of the increased background Gaussian noise contribution is reasonably weak for the range of S_t investigated, see panel c). In fact, the behavior of both T_u^p and T_u^f is only slightly perturbed even at the maximum value of D.

The monotonic decrease of the particle integral time scale is compatible with the *crossing trajectory effect* described in previous studies where gravity effects were included in the description of the transport of inertial particles (Csanady, 1963; Wang and Stock, 1993; Shao, 1995). In fact, for increasing inertia (S_t), the particle trajectories are facilitated to escape from the looping like Eulerian flow structures, typical of the Stokes drift, and loose correlation more rapidly, ultimately, leading to smaller integral time scales. However, we will see in the following that the scales T_u^p and T_u^f, calculated as in equations (9.11), mask an anisotropic behavior for both the particle and the *fluid seen by particles*.

Accelerations of inertial particles or fluid particles, which are directly related to the wave Stokes drift field, might provide some insight of particle diffusion. Panels b) and d) of Figure 9.12 report the acceleration integral scales T_a^p and T_a^f. We notice that the particle decorrelation times are no longer monotonic with S_t and less dependent on the wave parameters, except for Stokes numbers greater than 0.1. Moreover, T_a^f seems to be monotonically increasing with the Stokes number following, in this case, a power law of the kind $T_a^f \propto S_t$, with a similar goodness of fitting parameter. As for the velocity integral scales, the *fluid seen by particle* does not show any dependence on H/gT^2.

Contrary to the velocity integral scales, T_a^p is strongly modified by the background turbulence at least for $S_t < 0.03$, increasing the distance with T_a^f. At low levels of Brownian background and for $S_t < 0.05$, in fact, T_a^p and T_a^f are very close to each other. The intermediate decrease of T_a^p is probably due to the deviation of inertial particles from the swirling motion associated with

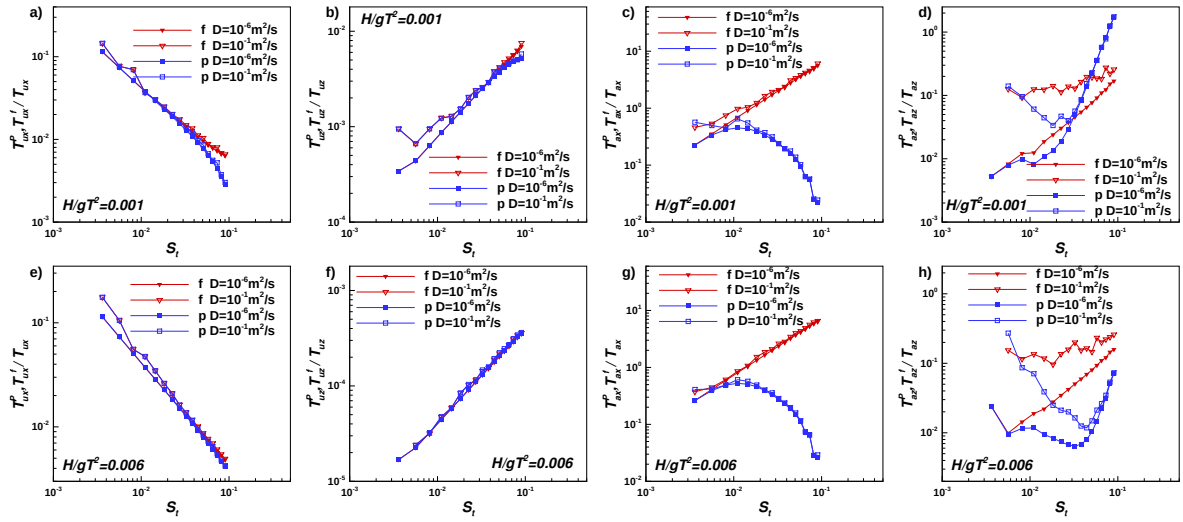

Figure 9.13: Velocity and acceleration integral scales for the single x and z components for two values of the diffusion coefficient D and for two wave conditions: a)-d) $H/gT^2 = 0.001$; e)-h) $H/gT^2 = 0.006$. p in the legend indicates particle integral scales and f indicates *fluid seen by particle*.

the fluid Stokes drift as the particle inertia increases. As S_t increases further, the particle path becomes insensitive to the flow structure, thus, the integral scales increase owing to the increase of the particle inertia.

Finally, in Figure 9.13 we show the variation of the velocity and acceleration components of the particle and *fluid seen by particle* integral scales for two values of the diffusion coefficient D and for two wave conditions, namely $H/gT^2 = 0.001$, panels a) - d) and $H/gT^2 = 0.006$ e) - h). Regarding the velocity integral scales, a similar behavior is found regardless of the wave parameters and the diffusion coefficient and it indicates a strong anisotropy between the longitudinal component T^p_{ux} and the vertical component T^p_{uz}. In fact, the vertical velocity time scale T^p_{uz} tends to increase with the Stokes number. However, its values are always less than the horizontal velocity time scale T^p_{ux}, thus, leading to the overall decay shown in Figure 9.12 panels a) and c). The strong similarity between the particle time scales and the *fluid seen by particle* ones is further confirmed and also the *fluid seen by particle* time scales show the same anisotropy.

The accelerations scales for both the particle and the *fluid seen by particle* show the greatest variability, especially in the vertical direction, see panels d) and h), where T^p_{az} and T^f_{az} are plotted. The vertical acceleration time scale seems to be very sensitive to the wave conditions and to the

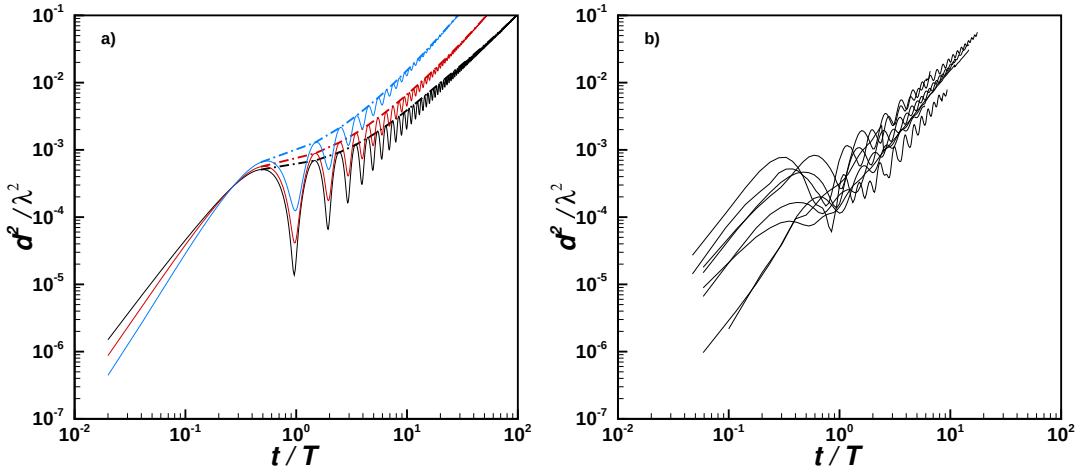

Figure 9.14: Non dimensional absolute dispersion d^2/λ^2 as a function of non dimensional time t/T. a) Results for $H/gT^2 = 0.004$ and three values of the Stokes number $S_t = 0.022, 0.044, 0.081$. b) Non dimensional absolute dispersion estimated from the experiments of section 9.1 for similar wave and particles parameters.

background Brownian noise, whereas its horizontal counterpart is much less influenced. It is indeed the rapid increase of T_{az}^p for Stokes greater than 0.1 that governs the overall trend shown in 9.12 panels b) and d), reaching also values larger than the fluid particle integral scale.

9.2.2 DISPERSION REGIMES

We are now interested in evaluating how the shape of the auto-correlation functions and the variability of the integral scales might influence the dispersion of heavy particles in the present flow conditions.

Firstly, we define the absolute dispersion of the heavy particles $d^2(t)$ as the ensemble average of the particle displacements with respect to an initial position, as the classical definition of the Taylor's theory. Assuming to deal with a certain number of particle trajectories released at some initial time t_0, the computation of the absolute dispersion could be performed accounting for or not the displacement of the center of mass of the considered ensemble of particles. In case where the mean drift of the center of mass is not considered, only the initial particle conditions are relevant and this strategy has been applied in several geophysical contexts, see LaCasce (2008); Stocchino et al. (2011); Mariano et al. (2016); Enrile et al. (2019) among others.

A different approach in the evaluation of the absolute dispersion involves the computation of

a mean drift related to the center of mass of a cluster of particles (LaCasce, 2008; Enrile et al., 2019). The total absolute dispersion is, therefore, evaluated removing at each time the position of the center of mass and the dispersion coefficient is simply the time derivative of $d^2(t)$.

For the present analysis, we preferred to use this second strategy of computation, which allows for an immediate removal of spurious effects related to mean drift that might lead to artifacts in the total dispersion.

It is worth recalling that Taylor (1921) found that for times smaller than the Lagrangian time scale a square time dependence of the absolute dispersion is recovered, i.e. $d^2(t) = \rho(0)t^2$, whereas for times greater than T^L a linear dependence in time is found ($d^2(t) = 2\rho(0)T^L t + \text{const}$). The latter implies the existence of diffusive (Brownian) regime characterized by a diffusion coefficient expressed as $K = \rho(0)T^L$. These two regimes, originally derived for fluid particles, have been found to be formally valid also for inertial particles (Csanady, 1963; Jung et al., 2008; Wetchagarun and Riley, 2010; Boi et al., 2018) and the existence of the diffusive regimes has been widely investigated in different contexts, owing to its extreme practical importance.

Taking advantage of the definition of K, several authors inferred the value of the coefficient providing a model for the particle velocity integral scale and, most of the time, comparing the value to the fluid value.

In the present case, the behavior of the non dimensional absolute dispersion d^2/λ^2 is affected by the combined effect of different time scales: the wave period, the convective time scale corresponding to the wave Stokes drift, the Stokes time and the integral time scales.

Figure 9.14 panel a) shows the total absolute dispersion normalized by the wavelength d^2/λ^2, versus the dimensionless time t/T. The oscillating character, imposed by the periodic Eulerian velocity field, is observed also in the time evolution of d^2/λ^2, similarly to the auto-correlation functions. The periodicity is well captured by the choice of T as time scale for the non-dimensional time. In panel a), we also report the values of d^2/λ^2 sampled every wave period, i.e. retaining just the oscillation peaks (dot dashed-lines), which will help in describing the dispersion regimes. Panel b) shows d^2/λ^2 evaluated from the experiments presented in De Leo et al. (2021) with similar wave and particle parameters for comparison. A similar oscillating total absolute dispersion is recovered also in the experiments.

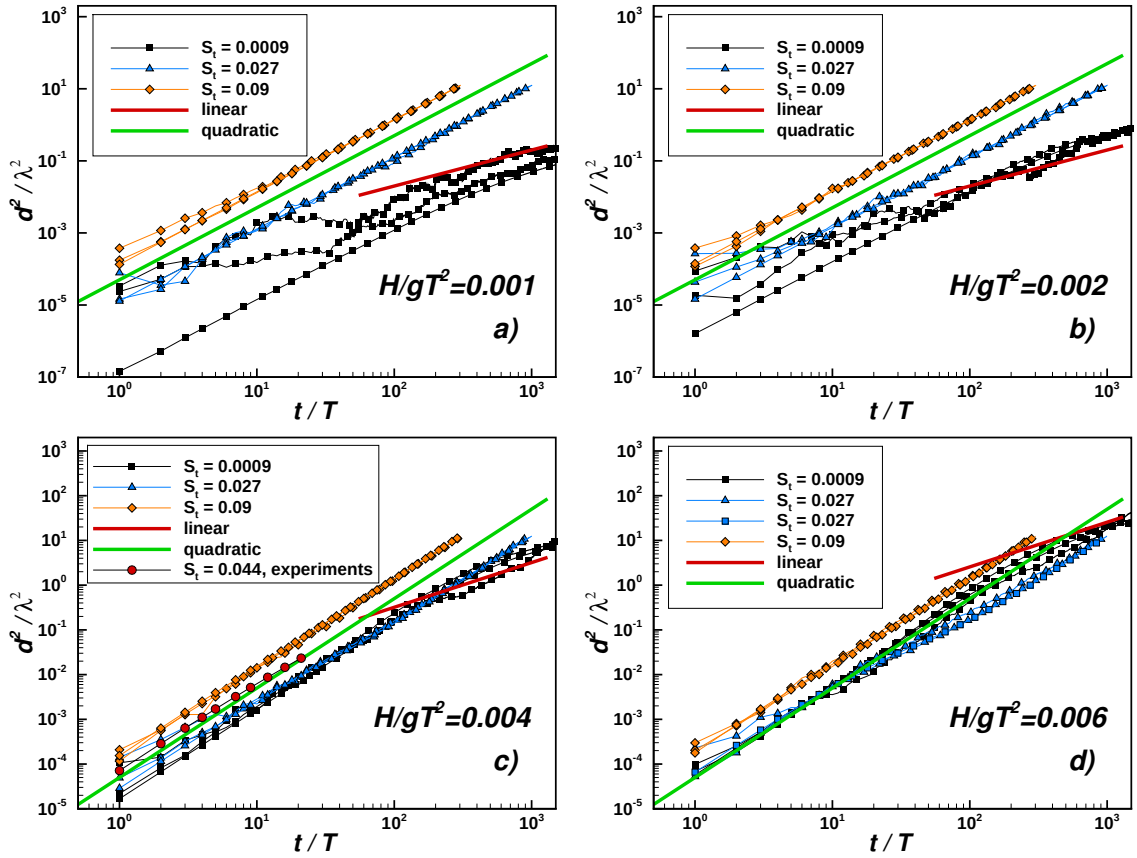

Figure 9.15: Normalized absolute dispersion for different wave parameter, Stokes number and turbulent diffusion. For each S_t three curves are plotted for $D = 10^{-6}, 10^{-3}, 10^{-1} \mathrm{m^2 s^{-1}}$. The green solid lines indicates $d^2/\lambda^2 \propto (t/T)^2$ whereas the red solid line stands for $d^2/\lambda^2 \propto (t/T)$.

Figure 9.15 shows wave period sampled d^2/λ^2 varying H/gT^2, for three different values of the Stokes number, $S_t = 0.0009, 0.027$ and 0.09.

The green solid line represents the ballistic regime, $d^2/\lambda^2 \propto (t/T)^2$, whereas the red solid line represents the diffusive regime $d^2/\lambda^2 \propto (t/T)$. Moreover, for the same S_t, we report the results obtained with three values of the turbulent diffusion D. For the case $H/gT^2 = 0.004$, panel c), the non dimensional absolute dispersion computed starting from the observed particle trajectories during the experiments (De Leo et al., 2021) is also reported for comparison. The experimental non dimensional absolute dispersion follows closely the ballistic regime and its values correctly fall between the two numerical simulations for Stokes number equal to 0.027 and 0.09. A first important observation is that no asymptotic diffusive regime exists in the range of parameters investigated (wave and particle parameters) with very few exceptions. This is in contrast with

what has been observed in other contexts of diffusion of heavy particles. In fact, a Brownian regime was observed already in the seminal paper by Csanady (1963), who retained gravity effect in his theory, claiming a difference between particle diffusion and fluid diffusion coefficient owing to crossing trajectories effect and continuity effect.

Moreover, the existence of a diffusion regime for heavy particles in turbulent flows without gravity effect or added-mass effect was always reported even for much higher Stokes numbers (Jung et al., 2008; Wetchagarun and Riley, 2010). Depending on the value of the Stokes number, the diffusion coefficient could also be increased by inertial effect, leading to values of the particle Schmidt number (ratio between particle long-time diffusion over fluid diffusion) between 0.1 and 2.

The present results, instead, show that a linear dependence of the absolute dispersion appears as a transient regime, only at very low Stokes number, between two quadratic regimes. Not surprisingly, a linear regime could be also recovered for very low values of the Stokes number and wave parameter and with a fairly high value of the Brownian process coefficient D of the order of $10^{-3}\mathrm{m}^2\mathrm{s}^{-1}$ or higher. However, as soon as S_t is grater than 0.002, the only regime clearly visible is the quadratic one. As the wave parameter increases, i.e. the wave Stokes drift is more intense, the behavior of all particles tends to collapse to very similar values, see panel d).

The generalization of the Taylor theory has been described by Boi et al. (2018) for several inertial forces and the buoyancy-forced case is particularly relevant for the present study. The asymptotic diffusion coefficient can be defined and it requires that the integral of the particle auto-correlation converges to a finite value. Super diffusive regimes, as the ballistic here described, is associated with a non convergent integral owing to a slowly decaying correlation, i.e. a long integral scale.

In the present case, the integral time scales, presented in Figure 9.12, show finite values, however, the shape of the correlation functions might be responsible for the disappearance of the Brownian regime. A possible physical explanation of the present results could be found in the settling process of heavy particles. The trajectory followed by the heavy particle could resemble the behavior described through the crossing trajectory effect introduced by Yudine (1959) and Csanady (1963) and resumed by Shao (1995) and Jung et al. (2008). Moreover, Santamaria et al.

(2013) aalready demonstrated with simple monochromatic wave that the net settling velocity is increased by the interplay of the wave Stokes drift and the particle inertia. This was further confirmed numerically by Stocchino et al. (2019) and exploited in section 9.1. The particle exits the fluid trajectory owing to inertial and gravity effect with an increased settling velocity, whereas it continues to be correlated and anti-correlated over a long time period.

Similar results are found by DiBenedetto et al. (2018) for the longitudinal dispersion and it was described as the settling regime. In other context, *super-diffusion processes* were associated with an overall auto-correlation function that exhibits a strong oscillation pattern, with a significant positive lobe that is more pronounced than the first negative lobe. The associated eddy dispersion was found to be faster than the typical diffusive spreading (Berloff et al., 2002; Veneziani et al., 2004). In the cited studies, the looping like auto-correlation was generated by the presence of coherent rotational flow structures that tended to maintain a positive and negative correlation over time, whereas the overall auto-correlation function decreased to zero. Anomalous diffusion regimes were also extensively studied (Castiglione et al., 1999) and linked to very strong correlations, which is the condition found in the present case.

CHAPTER 10

CONCLUSIONS

The present chapter reports both a laboratory investigation of the interaction between inertial heavy particles, as a realistic model for MPs particles, and the Stokes drift generated by sea waves, and a numerical simulation of a simplified transport model in order to study the transport of inertial particles owing to sea waves.

A series of experiments have been performed in a wave flume to cover a range of particle and wave parameters. The regular waves fall in intermediate and shallow depth conditions, with dimensionless sea state parameter H/gT^2 ranging from 0.001 to 0.006. Fixed-density but variably-sized PMMA particles were employed to cover a range of Stokes number between 0.0009 and 0.09, for a fixed value added-mass parameter of 0.9677.

The measurements reproduced typical behaviors predicted by previous theoretical and numerical models (Santamaria et al., 2013; Stocchino et al., 2019) confirming the validity of the model approaches. In addition, the results have shown a clear dependence of the net settling velocity not only on the particle characteristics, described by the particle Reynolds number, but also on the wave characteristics, through the sea state parameter H/gT^2. The inertial effects lead to a remarkable increasing of the particle settling velocity with respect to the one predicted by standard formulas validated in still fluids (Dietrich, 1982; Chubarenko et al., 2016; Khatmullina and Isachenko, 2017). The increased settling velocity is more evident as the particle Reynolds

number decrease, highlighting the tendency for larger particles to match more rapidly the still fluid settling velocity than smaller ones.
The present results have been interpreted in terms of a modified version of the standard Dietrich formula (Dietrich, 1982) allowing to account for wave dependency. The implementation of the latter formula into regional or larger scale transport model should improve the prediction of the fate of heavy MPs, including a simplified description of inertial effects.

Numerical simulation led on the conclusion that sea waves are able to generate a net Lagrangian transport by the Stokes drift, which is considered an important source of mass transport in coastal areas. We investigated the wave induced transport of heavy plastics, owing to their environmental importance, and discuss the possibility of the existence of an asymptotic diffusive regime. The present study is relevant in the understanding of micro-plastic transport models. In fact, among the different classes of plastic debris, particles with size smaller than a millimeter with a density higher than water are commonly observed (Kooi and Koelmans, 2019).
Most of the current numerical transport model (Eulerian or Lagrangian) disregard the inertial character of the micro-plastic particles and assume that it is possible to describe the fluxes of plastic particles in terms of an effective dispersion coefficient, implicitly assuming the existence of a diffusive regime (Isobe et al., 2014; Zhang and Savenije, 2017; Van Sebille et al., 2020).
On the contrary, the results of the present numerical simulations, performed using a wide range of the main parameters (waves and particles), show that, even for low Stokes numbers ($S_t < 0.36$), no asymptotic diffusive regime is observed except as a transient regime. The dispersion process remains always confined to a ballistic regime.
The effect of an added transport due to a background turbulence is also ineffective, even for turbulent coefficient of the order of 10^{-1} $\mathrm{m^2 s^{-1}}$, except for very low value of the Stokes number ($S_t < 0.005$) and wave parameter.
Heavy particles under the action of wave transport behave very differently from fluid particle showing correlations and integral scales far from the ones valid for passive particles. The looping like auto-correlations strongly influence the dispersion processes, inhibiting the establishment of a diffusive process following the classical Taylor's law. This conclusion is further demonstrated by the behavior of the absolute dispersion obtained from measured particle trajectories.

Note that the range of parameters investigated well represent the observations of microplastic in marine environment in terms of typical values of β and S_t (Kooi and Koelmans, 2019). Therefore, we question the adoption of Fickian-like law to model the fluxes of heavy particles, which requires a diffusive regime for time longer than the fluid integral time scale. Thus, more refined transport model would be required to correctly simulate the fate of heavy particles in coastal and open ocean circulations.

Future research will be dedicated to understand the role of the particle shapes and their importance on the net settling velocity as well as a wider range of the added-mass parameter. This aspect might be further complicated by the biofouling (Kooi et al., 2017; Porter et al., 2018; Kaiser et al., 2017) that is able to change the overall density and, then, the inertial properties of MPs. Moreover, several aspects need to be further investigated such as the role of a wave spectrum instead of a regular wave Eulerian field, a random distribution of particles described as a cluster and a more realistic non-spherical shape.
The results reported in Part 2 have been published in the following contributions:

- A. De Leo, L. Cutroneo, D. Sous, and A. Stocchino. Settling velocity of microplastics exposed to wave action. Journal of Marine Science and Engineering, 9(2):142, 2021.

- A. De Leo and A. Stocchino. Dispersion of heavy particles under sea waves. Physics of Fluids, accepted for publication.

BIBLIOGRAPHY

E. R. Abraham and M. M. Bowen. Chaotic stirring by a mesoscale surface-ocean flow. *Chaos: An Interdisciplinary Journal of Nonlinear Science*, 12(2):373–381, 2002.

R. Adrian, K. Christensen, and Z. Liu. Analysis and interpretation of istantaneous turbulent velocity fields. *Exp. in Fluids*, 29:275–290, 2000.

A. Alexakis and L. Biferale. Cascades and transitions in turbulent flows. *Physics Reports*, 767: 1–101, 2018.

M. R. Allshouse and T. Peacock. Lagrangian based methods for coherent structure detection. *Chaos: An Interdisciplinary Journal of Nonlinear Science*, 25(9):097617, 2015.

Y. Alosairi and N. Alsulaiman. Hydro-environmental processes governing the formation of hypoxic parcels in an inverse estuarine water body: Model validation and discussion. *Marine pollution bulletin*, 144:92–104, 2019.

H. Aluie, M. Hecht, and G. K. Vallis. Mapping the energy cascade in the north atlantic ocean: The coarse-graining approach. *Journal of Physical Oceanography*, 48(2):225–244, 2018.

M. Amin. On the conditions for classification of tides. *The International Hydrographic Review*, 1986.

R. Aris. *Vectors, tensors and the basic equations of fluid mechanics*. Dover Publications INC., New York, 1962.

V. Artale, G. Boffetta, A. Celani, M. Cencini, and A. Vulpiani. Dispersion of passive tracers in closed basins: Beyond the diffusion coefficient. *Physics of Fluids*, 9(11):3162–3171, 1997.

D. Aubrey and P. Speer. A study of non-linear tidal propagation in shallow inlet/estuarine systems part i: Observations. *Estuarine, Coastal and Shelf Science*, 21(2):185–205, 1985.

T. Awaji. Water mixing in a tidal current and the effect of turbulence on tidal exchange through a

strait. *Journal of Physical Oceanography*, 12(6):501–514, 1982.

T. Awaji, N. Imasato, and H. Kunishi. Tidal exchange through a strait: A numerical experiment using a simple model basin. *Journal of Physical Oceanography*, 10(10):1499–1508, 1980.

S. Ayyalasomayajula, A. Gylfason, L. R. Collins, E. Bodenschatz, and Z. Warhaft. Lagrangian measurements of inertial particle accelerations in grid generated wind tunnel turbulence. *Physical Review Letters*, 97(14):144507, 2006.

A. Babiano, C. Basdevant, P. Le Roy, and R. Sadourny. Relative dispersion in two-dimensional turbulence. *J. Fluid Mech.*, 214:535–557, 1990.

L. J. Baker and F. Coletti. Particle–fluid–wall interaction of inertial spherical particles in a turbulent boundary layer. *Journal of Fluid Mechanics*, 908, 2021.

A. Ballent, S. Pando, A. Purser, M. Juliano, and L. Thomsen. Modelled transport of benthic marine microplastic pollution in the nazaré canyon. *Biogeosciences*, 10(12):7957, 2013.

N. Banas, B. Hickey, P. MacCready, and J. Newton. Dynamics of willapa bay, washington: A highly unsteady, partially mixed estuary. *Journal of Physical Oceanography*, 34(11):2413–2427, 2004.

A. Barge and M. Gorokhovski. Acceleration of small heavy particles in homogeneous shear flow: direct numerical simulation and stochastic modelling of under-resolved intermittent turbulence. *Journal of Fluid Mechanics*, 892, 2020.

J. Bec, L. Biferale, G. Boffetta, A. Celani, M. Cencini, A. Lanotte, S. Musacchio, and F. Toschi. Acceleration statistics of heavy particles in turbulence. *Journal of Fluid Mechanics*, 550: 349–358, 2006.

J. Bec, L. Biferale, M. Cencini, A. Lanotte, S. Musacchio, and F. Toschi. Heavy particle concentration in turbulence at dissipative and inertial scales. *Physical review letters*, 98(8):084502, 2007.

J. Bec, L. Biferale, A. Lanotte, A. Scagliarini, and F. Toschi. Turbulent pair dispersion of inertial particles. *Journal of Fluid Mechanics*, 645:497–528, 2010.

S. Beerens, H. Ridderinkhof, and J. Zimmerman. An analytical study of chaotic stirring in tidal areas. *Chaos, Solitons & Fractals*, 4(6):1011–1029, 1994.

S. J. Benavides and A. Alexakis. Critical transitions in thin layer turbulence. *Journal of Fluid Mechanics*, 822:364–385, 2017.

A. Bennett. Relative dispersion: Local and nonlocal dynamics. *J. Atm Sc.*, 41:1881–1886, 1984.

M. Bergmann, V. Wirzberger, T. Krumpen, C. Lorenz, S. Primpke, M. B. Tekman, and G. Gerdts. High quantities of microplastic in arctic deep-sea sediments from the hausgarten observatory. *Environmental Science & Technology*, 51(19):11000–11010, 2017.

T. Berk and F. Coletti. Dynamics of small heavy particles in homogeneous turbulence: a lagrangian experimental study. *Journal of Fluid Mechanics*, 917, 2021.

P. S. Berloff, J. C. McWilliams, and A. Bracco. Material transport in oceanic gyres. part i: Phenomenology. *Journal of Physical Oceanography*, 32(3):764–796, 2002.

F. J. Beron-Vera, M. J. Olascoaga, and P. Miron. Building a maxey–riley framework for surface ocean inertial particle dynamics. *Physics of Fluids*, 31(9):096602, 2019.

G. Besio, A. Stocchino, S. Angiolani, and M. Brocchini. Transversal and longitudinal mixing in compound channels. *Water Resources Research*, 48(12), 2012.

L. Biferale, G. Boffetta, A. Celani, B. Devenish, A. Lanotte, and F. Toschi. Lagrangian statistics of particle pairs in homogeneous isotropic turbulence. *Physics of Fluids*, 17(11):115101, 2005.

G. Boffetta. Energy and enstrophy fluxes in the double cascade of two-dimensional turbulence. *Journal of Fluid Mechanics*, 589:253–260, 2007.

G. Boffetta, G. Lacorata, G. Redaelli, and A. Vulpiani. Detecting barriers to transport: A review of different techniques. *Physica D*, 159:58–70, 2001.

G. Boffetta, F. De Lillo, and S. Musacchio. Shell model for quasi-two-dimensional turbulence. *Physical Review E*, 83(6):066302, 2011.

S. Boi, M. M. Afonso, and A. Mazzino. Anomalous diffusion of inertial particles in random parallel flows: theory and numerics face to face. *Journal of Statistical Mechanics: Theory and Experiment*, 2015(10):P10023, 2015.

S. Boi, A. Mazzino, and G. Lacorata. Explicit expressions for eddy-diffusivity fields and effective large-scale advection in turbulent transport. *Journal of Fluid Mechanics*, 795:524–548, 2016.

S. Boi, A. Mazzino, P. Muratore-Ginanneschi, and S. Olivieri. Generalization of taylor's formula to particles of arbitrary inertia. *Physical Review Fluids*, 3(10):104501, 2018.

J. Branyon, A. Valle-Levinson, I. Mariño-Tapia, and C. Enriquez. Intratidal and residual flows around inlets of a reef lagoon. *Estuaries and Coasts*, pages 1–15, 2021.

M. Brocchini and M. Colombini. A note on the decay of vorticity in shallow flow calculations. *Physics of Fluids*, 16(7):2469–2475, 2004.

K. Brunner, T. Kukulka, G. Proskurowski, and K. Law. Passive buoyant tracers in the ocean surface boundary layer: 2. observations and simulations of microplastic marine debris. *Journal of Geophysical Research: Oceans*, 120(11):7559–7573, 2015.

H. Cai, H. H. Savenije, and M. Toffolon. A new analytical framework for assessing the effect of sea-level rise and dredging on tidal damping in estuaries. *Journal of Geophysical Research: Oceans*, 117(C9), 2012.

W. Cameron and D. Pritchard. Estuaries. in 'the sea, vol. 2'.(ed. mn hill.) pp. 306–324, 1963.

P. Castiglione, A. Mazzino, P. Muratore-Ginanneschi, and A. Vulpiani. On strong anomalous diffusion. *Physica D: Nonlinear Phenomena*, 134(1):75–93, 1999.

M. Cencini and A. Vulpiani. Finite size lyapunov exponent: review on applications. *Journal of Physics A: Mathematical and Theoretical*, 46(25):254019, 2013.

M. Cencini, J. Bec, L. Biferale, G. Boffetta, A. Celani, A. Lanotte, S. Musacchio, and F. Toschi. Dynamics and statistics of heavy particles in turbulent flows. *Journal of Turbulence*, (7):N36, 2006.

K. W. Chau. Transverse mixing coefficient measurements in an open rectangular channel. *Advances in Environmental Research*, 4(4):287–294, 2000.

M. S. Chong, A. E. Perry, and B. J. Cantwell. A general classification of three-dimensional flow fields. *Physics of Fluids A: Fluid Dynamics*, 2(5):765–777, 1990.

I. Chubarenko, A. Bagaev, M. Zobkov, and E. Esiukova. On some physical and dynamical properties of microplastic particles in marine environment. *Marine pollution bulletin*, 108(1-2): 105–112, 2016.

R. Clift, J. Grace, and M. Weber. Nonspherical rigid particles at higher reynolds numbers. *Bubbles Drops and Particles*, pages 142–168, 1978.

T. F. Coleman and Y. Li. An interior trust region approach for nonlinear minimization subject to bounds. *SIAM Journal on optimization*, 6(2):418–445, 1996.

G. Csanady. Turbulent diffusion of heavy particles in the atmosphere. *Journal of Atmospheric Sciences*, 20(3):201–208, 1963.

A. Cucco, G. Umgiesser, C. Ferrarin, A. Perilli, D. M. Canu, and C. Solidoro. Eulerian and lagrangian transport time scales of a tidal active coastal basin. *Ecological Modelling*, 220(7): 913–922, 2009.

L. Cutroneo, A. Reboa, G. Besio, F. Borgogno, L. Canesi, S. Canuto, M. Dara, F. Enrile, I. Forioso, G. Greco, V. Lenoble, A. Malatesta, S. Mounier, M. Petrillo, R. Rovetta, A. Stocchino, G. Tesan, Javier Vagge, and M. Capello. Microplastics in seawater: sampling strategies, laboratory methodologies, and identification techniques applied to port environment. *Environmental Science and Pollution Research*, pages 1–15, 2020.

P. A. Davies, J. M. Dakin, and R. A. Falconer. Eddy formation behind a coastal headland. *Journal of Coastal Research*, pages 154–167, 1995.

A. De Leo, L. Cutroneo, D. Sous, and A. Stocchino. Settling velocity of microplastics exposed to wave action. *Journal of Marine Science and Engineering*, 9(2):142, 2021.

R. G. Dean and R. A. Dalrymple. *Water wave mechanics for engineers and scientists*, volume 2. World Scientific Publishing Company, 1991.

M. H. DiBenedetto, N. T. Ouellette, and J. R. Koseff. Transport of anisotropic particles under waves. *Journal of Fluid Mechanics*, 837:320–340, 2018.

W. E. Dietrich. Settling velocity of natural particles. *Water resources research*, 18(6):1615–1626, 1982.

F. d'Ovidio, J. Isern-Fontanet, C. López, E. Hernández-García, and E. García-Ladona. Comparison between eulerian diagnostics and finite-size lyapunov exponents computed from altimetry in the algerian basin. *Deep Sea Research Part I: Oceanographic Research Papers*, 56(1):15–31, 2009.

D. Drevard, V. Rey, and P. Fraunié. Partially standing wave measurement in the presence of steady current by use of coincident velocity and/or pressure data. *Coastal engineering*, 56(9): 992–1001, 2009.

Dronkers. *Estuarine dispersion: dye experiments in the Eastern Scheldt scale model*. http://www.coastalwiki.org/wiki/Estuarine dispersion: dye experiments in the Eastern Scheldt scale mode, 2019.

Y. Drossinos and M. W. Reeks. Brownian motion of finite-inertia particles in a simple shear flow.

Physical Review E, 71(3):031113, 2005.

P. C. Du Toit. *Transport and separatrices in time-dependent flows*. California Institute of Technology, 2010.

D. Elhmaïdi, A. Provenzale, and A. Babiano. Elementary topology of two-dimensional turbulence from a lagrangian viewpoint and single-particle dispersion. *J. Fluid Mech.*, 257:533–558, 1993.

F. Enrile, G. Besio, and A. Stocchino. Shear and shearless lagrangian structures in compound channels. *Advances in Water Resources*, 113:141–154, 2018a.

F. Enrile, G. Besio, A. Stocchino, M. Magaldi, C. Mantovani, S. Cosoli, R. Gerin, and P. Poulain. Evaluation of surface lagrangian transport barriers in the gulf of trieste. *Continental Shelf Research*, 167:125–138, 2018b.

F. Enrile, G. Besio, A. Stocchino, and M. G. Magaldi. Influence of initial conditions on absolute and relative dispersion in semi-enclosed basins. *PloS one*, 14(7), 2019.

F. Enrile, G. Besio, and A. Stocchino. Eulerian spectrum of finite-time lyapunov exponents in compound channels. *Meccanica*, 55(9):1821–1828, 2020.

J. Er-El and R. Peskin. Relative diffusion of constant-level balloons in the suthern hemisphere. *J. Atm Sc.*, 38:2264–2274, 1981.

L. Fang and N. T. Ouellette. Advection and the efficiency of spectral energy transfer in two-dimensional turbulence. *Physical review letters*, 117(10):104501, 2016.

L. Fang, S. Balasuriya, and N. T. Ouellette. Local linearity, coherent structures, and scale-to-scale coupling in turbulent flow. *Physical Review Fluids*, 4(1):014501, 2019.

M. Farazmand and T. Sapsis. Surface waves enhance particle dispersion. *Fluids*, 4(1):55, 2019.

M. Figari and M. Altosole. Dynamic behaviour and stability of marine propulsion systems. *Proceedings of The Institution of Mechanical Engineers Part M-journal of Engineering for The Maritime Environment*, 221:187–205, 12 2007. doi: 10.1243/14750902JEME58.

H. B. Fischer, J. E. List, C. R. Koh, J. Imberger, and N. H. Brooks. *Mixing in inland and coastal waters*. Academic press, 1979.

K. O. Fong, O. Amili, and F. Coletti. Velocity and spatial distribution of inertial particles in a turbulent channel flow. *Journal of Fluid Mechanics*, 872:367–406, 2019.

A. B. Fortunato and A. Oliveira. Influence of intertidal flats on tidal asymmetry. *Journal of*

Coastal Research, 21(5 (215)):1062–1067, 2005.

C. T. Friedrichs and D. G. Aubrey. Non-linear tidal distortion in shallow well-mixed estuaries: a synthesis. *Estuarine, Coastal and Shelf Science*, 27(5):521–545, 1988.

C. T. Friedrichs and D. G. Aubrey. Tidal propagation in strongly convergent channels. *Journal of Geophysical Research: Oceans*, 99(C2):3321–3336, 1994.

C. T. Friedrichs and O. S. Madsen. Nonlinear diffusion of the tidal signal in frictionally dominated embayments. *Journal of Geophysical Research: Oceans*, 97(C4):5637–5650, 1992.

L. Geng, Z. Gong, Z. Zhou, S. Lanzoni, and A. D'Alpaos. Assessing the relative contributions of the flood tide and the ebb tide to tidal channel network dynamics. *Earth Surface Processes and Landforms*, 45(1):237–250, 2020.

S. Gerashchenko, N. Sharp, S. Neuscamman, and Z. Warhaft. Lagrangian measurements of inertial particle accelerations in a turbulent boundary layer. *Journal of fluid mechanics*, 617: 255, 2008.

M. Germano. Turbulence: the filtering approach. *Journal of Fluid Mechanics*, 238:325–336, 1992.

W. R. Geyer and P. MacCready. The estuarine circulation. *Annual review of fluid mechanics*, 46: 175–197, 2014.

J. I. A. Gisen and H. H. Savenije. Estimating bankfull discharge and depth in ungauged estuaries. *Water Resources Research*, 51(4):2298–2316, 2015.

M. A. Green, C. W. Rowley, and G. Haller. Detection of lagrangian coherent structures in three-dimensional turbulence. *Journal of Fluid Mechanics*, 572:111–120, 2007.

K. Gustavsson and B. Mehlig. Statistical models for spatial patterns of heavy particles in turbulence. *Advances in Physics*, 65(1):1–57, 2016.

G. Haller. A variational theory of hyperbolic lagrangian coherent structures. *Physica D: Nonlinear Phenomena*, 240(7):574–598, 2011.

G. Haller. Lagrangian coherent structures. *Annual Review of Fluid Mechanics*, 47:137–162, 2015.

G. Haller and F. J. Beron-Vera. Geodesic theory of transport barriers in two-dimensional flows. *Physica D: Nonlinear Phenomena*, 241(20):1680–1702, 2012.

G. Haller and G. Yuan. Lagrangian coherent structures and mixing in two-dimensional turbulence. *Physica D: Nonlinear Phenomena*, 147(3-4):352–370, 2000.

D. V. Hansen and M. Rattray Jr. New dimensions in estuary classification 1. *Limnology and oceanography*, 11(3):319–326, 1966.

N. B. Hartmann, T. Huffer, R. C. Thompson, M. Hassellov, A. Verschoor, A. E. Daugaard, S. Rist, T. Karlsson, N. Brennholt, and M. Cole. Are we speaking the same language? recommendations for a definition and categorization framework for plastic debris. *Environmental science & technology*, 53:1039–1047, 2019.

A. C. Haza, A. C. Poje, T. M. Özgökmen, and P. Martin. Relative dispersion from a high-resolution coastal model of the adriatic sea. *Ocean Modelling*, 22(1-2):48–65, 2008.

Z. HE, Z. LIU, S. CHEN, L. WENG, and C. ZHENG. Direct numerical simulation of particle behaviorin homogeneous isotropic turbulence [j]. *Journal of Chemical Industry and Engineering (China)*, 2, 2006.

C. Herbert. An introduction to fluid turbulence.

V. Hidalgo-Ruz, L. Gutow, R. C. Thompson, and M. Thiel. Microplastics in the marine environment: a review of the methods used for identification and quantification. *Environmental science & technology*, 46(6):3060–3075, 2012.

A. Isobe, K. Kubo, Y. Tamura, E. Nakashima, N. Fujii, et al. Selective transport of microplastics and mesoplastics by drifting in coastal waters. *Marine pollution bulletin*, 89(1-2):324–330, 2014.

I. Jalón-Rojas, W. Xiao-Hua, and E. Fredj. On the importance of a three-dimensional approach for modelling the transport of neustic microplastics. *Ocean Science*, 15(3):717–724, 2019.

D. A. Jay. Green's law revisited: Tidal long-wave propagation in channels with strong topography. *Journal of Geophysical Research: Oceans*, 96(C11):20585–20598, 1991.

G. Jirka. Large scale flow structures and mixing processes in shallow flows. *J. Hydr. Res.*, 39: 567–573, 2001.

J. Jung, K. Yeo, and C. Lee. Behavior of heavy particles in isotropic turbulence. *Physical Review E*, 77(1):016307, 2008.

D. Kaiser, N. Kowalski, and J. J. Waniek. Effects of biofouling on the sinking behavior of microplastics. *Environmental Research Letters*, 12(12):124003, 2017.

J. Kang and K. Jun. Flood and ebb dominance in estuaries in korea. *Estuarine, Coastal and Shelf*

Science, 56(1):187–196, 2003.

D. H. Kelley and N. T. Ouellette. Spatiotemporal persistence of spectral fluxes in two-dimensional weak turbulence. *Physics of Fluids*, 23(11):115101, 2011.

L. Khatmullina and I. Isachenko. Settling velocity of microplastic particles of regular shapes. *Marine pollution bulletin*, 114(2):871–880, 2017.

A. N. Kolmogorov. The local structure of turbulence in incompressible viscous fluid for very large reynolds numbers. *Cr Acad. Sci. URSS*, 30:301–305, 1941.

M. Kooi and A. A. Koelmans. Simplifying microplastic via continuous probability distributions for size, shape, and density. *Environmental Science & Technology Letters*, 6(9):551–557, 2019.

M. Kooi, E. H. v. Nes, M. Scheffer, and A. A. Koelmans. Ups and downs in the ocean: effects of biofouling on vertical transport of microplastics. *Environmental science & technology*, 51(14): 7963–7971, 2017.

H. Kraichnan. Dispersion of particle pairs in homogeneous turbulence. *Phys. Fluids*, 9:1937–1943, 1966.

T. Kukulka and K. Brunner. Passive buoyant tracers in the ocean surface boundary layer: 1. influence of equilibrium wind-waves on vertical distributions. *Journal of Geophysical Research: Oceans*, 120(5):3837–3858, 2015.

T. Kukulka, G. Proskurowski, S. Morét-Ferguson, D. Meyer, and K. Law. The effect of wind mixing on the vertical distribution of buoyant plastic debris. *Geophysical Research Letters*, 39(7), 2012.

N. Kumar, D. L. Cahl, S. C. Crosby, and G. Voulgaris. Bulk versus spectral wave parameters: Implications on stokes drift estimates, regional wave modeling, and hf radars applications. *Journal of Physical Oceanography*, 47(6):1413–1431, 2017.

Kusumoto. *Laboratory Experiments of Tidal Dispersion around Irregular Boundaries*. Phd Thesis, 2008.

J. LaCasce. Statistics from lagrangian observations. *Progress in Oceanography*, 77:129, 2008.

S. Lanzoni and G. Seminara. On tide propagation in convergent estuaries. *Journal of Geophysical Research: Oceans*, 103(C13):30793–30812, 1998.

K. L. Law. Plastics in the marine environment. *Annual review of marine science*, 9:205–229, 2017.

S.-H. Lee and Y.-S. Chang. Classification of the global tidal types based on auto-correlation analysis. *Ocean Science Journal*, 54(2):279–286, 2019.

F. Lekien, C. Coulliette, A. Mariano, E. Ryan, L. Shay, G. Haller, and J. Marsden. Pollution release tied to invariant manifolds: A case study for the coast of florida. *Phys. D*, 210:1–20, 2005.

B. LeMéhauté. *An introduction to hydrodynamics and water waves*, volume 52. Environmental Science Servies Administration, 1969.

R. E. Lewis and R. J. Uncles. Factors affecting longitudinal dispersion in estuaries of different scale. *Ocean Dynamics*, 53(3):197–207, 2003.

Y. Liao and N. T. Ouellette. Spatial structure of spectral transport in two-dimensional flow. *Journal of Fluid Mechanics*, 725:281–298, 2013.

Y. Liao and N. T. Ouellette. Geometry of scale-to-scale energy and enstrophy transport in two-dimensional flow. *Physics of Fluids*, 26(4):045103, 2014.

Y. Liao and N. T. Ouellette. Correlations between the instantaneous velocity gradient and the evolution of scale-to-scale fluxes in two-dimensional flow. *Physical Review E*, 92(3):033017, 2015a.

Y. Liao and N. T. Ouellette. Long-range ordering of turbulent stresses in two-dimensional flow. *Physical Review E*, 91(6):063004, 2015b.

J. Lin. Relative dispersion in the enstrophy cascading inertial range of homogeneous two dimensional turbulence. *J. Atmos. Sci.*, 29:394–396, 1972.

S. Liubartseva, G. Coppini, R. Lecci, and S. Creti. Regional approach to modeling the transport of floating plastic debris in the adriatic sea. *Marine pollution bulletin*, 103(1-2):115–127, 2016.

S. Liubartseva, G. Coppini, R. Lecci, and E. Clementi. Tracking plastics in the mediterranean: 2d lagrangian model. *Marine pollution bulletin*, 129(1):151–162, 2018.

L. Lourenco. True resolution piv: a mesh-free second order accurate algorithm. In *10th Int. Symp. on Applications of Laser Techniques in Fluid Mechanics (Lisbon), 2000*, 2000.

P. MacCready. Estuarine adjustment to changes in river flow and tidal mixing. *Journal of Physical Oceanography*, 29(4):708–726, 1999.

P. MacCready and W. R. Geyer. Advances in estuarine physics. *Annual Review of Marine Science*,

2:35–58, 2010.

A. J. Mariano, E. Ryan, H. Huntley, L. Laurindo, E. Coelho, A. Griffa, T. Özgökmen, M. Berta, D. Bogucki, S. S. Chen, et al. Statistical properties of the surface velocity field in the northern gulf of mexico sampled by glad drifters. *Journal of Geophysical Research: Oceans*, 121(7): 5193–5216, 2016.

M. Mathur, G. Haller, T. Peacock, J. E. Ruppert-Felsot, and H. L. Swinney. Uncovering the lagrangian skeleton of turbulence. *Physical Review Letters*, 98(14):144502, 2007.

M. Maxey and J. Riley. Equation of motion for a small rigid sphere in a nonuniform flow. *The Physics of Fluids*, 26(4):883–889, 1983.

N. Maximenko, J. Hafner, and P. Niiler. Pathways of marine debris derived from trajectories of lagrangian drifters. *Marine pollution bulletin*, 65(1-3):51–62, 2012.

K. J. McDermid and T. L. McMullen. Quantitative analysis of small-plastic debris on beaches in the hawaiian archipelago. *Marine pollution bulletin*, 48(7-8):790–794, 2004.

S. G. Monismith, W. Kimmerer, J. R. Burau, and M. T. Stacey. Structure and flow-induced variability of the subtidal salinity field in northern san francisco bay. *Journal of physical Oceanography*, 32(11):3003–3019, 2002.

L. F. Moody. Friction factors for pipe flow. *Trans. Asme*, 66:671–684, 1944.

J. J. Moré and D. C. Sorensen. Computing a trust region step. *SIAM Journal on Scientific and Statistical Computing*, 4(3):553–572, 1983.

S. Morét-Ferguson, K. L. Law, G. Proskurowski, E. K. Murphy, E. E. Peacock, and C. M. Reddy. The size, mass, and composition of plastic debris in the western north atlantic ocean. *Marine Pollution Bulletin*, 60(10):1873–1878, 2010.

F. Nicolau del Roure, S. A. Socolofsky, and K.-A. Chang. Structure and evolution of tidal starting jet vortices at idealized barotropic inlets. *Journal of Geophysical Research: Oceans*, 114(C5), 2009.

V. Nikora, R. Nokes, W. Veale, M. Davidson, and G. Jirka. Large-scale turbulent structure of uniform shallow free-surface flows. *Environ Fluid Mech.*, 7:159–172, 2007.

A. Okubo. Horizontal dispersion of floatable particles in the vicinity of velocity singularities such as convergences. *Depp-Sea Res.*, 17:445–454, 1970.

M. J. Olascoaga and G. Haller. Forecasting sudden changes in environmental pollution patterns. *Proceedings of the National Academy of Sciences*, 109(13):4738–4743, 2012.

S. Orre, B. Gjevik, and J. LaCasce. Characterizing chaotic dispersion in a coastal tidal model. *Continental Shelf Research*, 26:1360–1374, 2006.

D. Peregrine. Interaction of water waves and currents. In *Advances in applied mechanics*, volume 16, pages 9–117. Elsevier, 1976.

PlasticsEurope. Annual report 2018 "plastics – the facts 2018. an analysis of european latest plastics production, demand and waste data". Technical report, Brussels – Belgium, 2018.

S. B. Pope. *Turbulent flows*. Cambridge university press, 2000.

A. Porter, B. P. Lyons, T. S. Galloway, and C. Lewis. Role of marine snows in microplastic fate and bioavailability. *Environmental science & technology*, 52(12):7111–7119, 2018.

J. Pozorski and J.-P. Minier. On the lagrangian turbulent dispersion models based on the langevin equation. *International Journal of Multiphase Flow*, 24(6):913–945, 1998.

J. Pozorski and J.-P. Minier. Probability density function modeling of dispersed two-phase turbulent flows. *Physical Review E*, 59(1):855, 1999.

A. Provenzale. Transport by coherent barotropic vortices. *Ann. Rev. Fluid Mech.*, 31:55–93, 1999.

M. Raffel, C. E. Willert, J. Kompenhans, et al. *Particle image velocimetry: a practical guide*, volume 2. Springer, 1998.

M. Reeks. The relationship between brownian motion and the random motion of small particles in a turbulent flow. *The Physics of fluids*, 31(6):1314–1316, 1988.

Y. Ren, B. Lin, J. Sun, and S. Pan. Predicting water age distribution in the pearl river estuary using a three-dimensional model. *Journal of Marine Systems*, 139:276–287, 2014.

V. Rey, R. Capobianco, and C. Dulou. Wave scattering by a submerged plate in presence of a steady uniform current. *Coastal Engineering*, 47(1):27–34, 2002.

S. Rezania, J. Park, M. F. M. Din, S. M. Taib, A. Talaiekhozani, K. K. Yadav, and H. Kamyab. Microplastics pollution in different aquatic environments and biota: A review of recent studies. *Marine pollution bulletin*, 133:191–208, 2018.

H. Ridderinkhof and J. Zimmerman. Chaotic stirring in a tidal system. *Science*, 258(5085): 1107–1111, 1992.

M. Rivera, H. Aluie, and R. Ecke. The direct enstrophy cascade of two-dimensional soap film flows. *Physics of Fluids*, 26(5):055105, 2014.

M. Rosti, S. Olivieri, M. Cavaiola, A. Seminara, and A. Mazzino. Fluid dynamics of covid-19 airborne infection suggests urgent data for a scientific design of social distancing. *Scientific reports*, 10(1):1–9, 2020.

F. Santamaria, G. Boffetta, M. M. Afonso, A. Mazzino, M. Onorato, and D. Pugliese. Stokes drift for inertial particles transported by water waves. *EPL (Europhysics Letters)*, 102(1):14003, 2013.

H. H. Savenije. Determination of estuary parameters on basis of lagrangian analysis. *Journal of Hydraulic Engineering*, 119(5):628–642, 1993.

G. Seminara, S. Lanzoni, N. Tambroni, and M. Toffolon. How long are tidal channels? *Journal of Fluid Mechanics*, 643:479, 2010.

S. C. Shadden, F. Lekien, and J. E. Marsden. Definition and properties of lagrangian coherent structures from finite-time lyapunov exponents in two-dimensional aperiodic flows. *Physica D: Nonlinear Phenomena*, 212(3-4):271–304, 2005.

Y.-P. Shao. A lagrangian stochastic model for nonpassive particle diffusion in turbulent flows. *Mathematical and computer modelling*, 21(9):31–37, 1995.

K. Shiono and D. Knight. Turbulent open-channel flows with variable depth across the channel. *J. Fluid Mech.*, 222:617–646, 1991.

R. P. Signell and W. R. Geyer. Transient eddy formation around headlands. *Journal of Geophysical Research: Oceans*, 96(C2):2561–2575, 1991.

T. Steihaug. The conjugate gradient method and trust regions in large scale optimization. *SIAM Journal on Numerical Analysis*, 20(3):626–637, 1983.

A. Stocchino and M. Brocchini. Horizontal mixing of quasi-uniform, straight, compound channel flows. *J. Fluid Mech.*, 643:425–435, 2010.

A. Stocchino, G. Besio, S. Angiolani, and M. Brocchini. Lagrangian mixing in straight compound channels. *Journal of Fluid Mechanics*, 675:168–198, 2011.

A. Stocchino, F. De Leo, and G. Besio. Sea waves transport of inertial micro-plastics: Mathematical model and applications. *Journal of Marine Science and Engineering*, 7(12):467, 2019.

G. G. Stokes et al. *On the effect of the internal friction of fluids on the motion of pendulums*, volume 9. Pitt Press Cambridge, 1851.

H. Stommel and H. G. Farmer. On the nature of estuarine circulation. part i (chapters 3 and 4). Technical report, 1952.

G. Suaria, V. Perold, J. R. Lee, F. Lebouard, S. Aliani, and P. G. Ryan. Floating macro-and microplastics around the southern ocean: Results from the antarctic circumnavigation expedition. *Environment International*, 136:105494, 2020.

W. Tang, M. Mathur, G. Haller, D. C. Hahn, and F. H. Ruggiero. Lagrangian coherent structures near a subtropical jet stream. *Journal of the Atmospheric Sciences*, 67(7):2307–2319, 2010.

G. Taylor. Diffusion by continuous movement. *Proc. Lond. Math. Soc.*, 20:196–212, 1921.

H. Tennekes, J. L. Lumley, J. L. Lumley, et al. *A first course in turbulence*. MIT press, 1972.

J.-L. Thiffeault and A. H. Boozer. Geometrical constraints on finite-time lyapunov exponents in two and three dimensions. *Chaos: An Interdisciplinary Journal of Nonlinear Science*, 11(1): 16–28, 2001.

M. Toffolon, G. Vignoli, and M. Tubino. Relevant parameters and finite amplitude effects in estuarine hydrodynamics. *Journal of Geophysical Research: Oceans*, 111(C10), 2006.

M. Tsimplis, R. Proctor, and R. Flather. A two-dimensional tidal model for the mediterranean sea. *Journal of Geophysical Research: Oceans*, 100(C8):16223–16239, 1995.

G. Umgiesser, C. Ferrarin, A. Cucco, F. De Pascalis, D. Bellafiore, M. Ghezzo, and M. Bajo. Comparative hydrodynamics of 10 mediterranean lagoons by means of numerical modeling. *Journal of Geophysical Research: Oceans*, 119(4):2212–2226, 2014.

A. Valle-Levinson. *Contemporary issues in estuarine physics*. Cambridge University Press, 2010.

A. Valle-Levinson. Dynamics-based classification of semienclosed basins. *Regional Studies in Marine Science*, page 101866, 2021.

A. Valle-Levinson, G. Gutierrez de Velasco, A. Trasviña, A. J. Souza, R. Durazo, and A. J. Mehta. Residual exchange flows in subtropical estuaries. *Estuaries and coasts*, 32(1):54–67, 2009.

M. Van der Vegt, H. Schuttelaars, and H. De Swart. Modeling the equilibrium of tide-dominated ebb-tidal deltas. *Journal of Geophysical Research: Earth Surface*, 111(F2), 2006.

E. Van Sebille, S. M. Griffies, R. Abernathey, T. P. Adams, P. Berloff, A. Biastoch, B. Blanke,

E. P. Chassignet, Y. Cheng, C. J. Cotter, et al. Lagrangian ocean analysis: Fundamentals and practices. *Ocean Modelling*, 121:49–75, 2018.

E. Van Sebille, S. Aliani, K. L. Law, N. Maximenko, J. M. Alsina, A. Bagaev, M. Bergmann, B. Chapron, I. Chubarenko, A. Cózar, et al. The physical oceanography of the transport of floating marine debris. *Environmental Research Letters*, 15(2):023003, 2020.

M. Veneziani, A. Griffa, A. M. Reynolds, and A. J. Mariano. Oceanic turbulence and stochastic models from subsurface lagrangian data for the northwest atlantic ocean. *Journal of physical oceanography*, 34(8):1884–1906, 2004.

D. P. Viero and A. Defina. Water age, exposure time, and local flushing time in semi-enclosed, tidal basins with negligible freshwater inflow. *Journal of Marine Systems*, 156:16–29, 2016.

P. Villarrubia-Gómez, S. E. Cornell, and J. Fabres. Marine plastic pollution as a planetary boundary threat–the drifting piece in the sustainability puzzle. *Marine Policy*, 96:213–220, 2018.

C. V. Vouriot, A. Angeloudis, S. C. Kramer, and M. D. Piggott. Fate of large-scale vortices in idealized tidal lagoons. *Environmental Fluid Mechanics*, 19(2):329–348, 2019.

K. Waldschlager and H. Schuttrumpf. Effects of particle properties on the settling and rise velocities of microplastics in freshwater under laboratory conditions. *Environmental science & technology*, 53(4):1958–1966, 2019.

L.-P. Wang and D. E. Stock. Dispersion of heavy particles by turbulent motion. *Journal of Atmospheric Sciences*, 50(13):1897–1913, 1993.

G. Webel and M. Schatzmann. Transverse mixing in open channel flow. *Journal of Hydraulic Engineering*, 110(4):423–435, 1984.

J. Weiss. The dynamics of enstrophy transfer in two-dimensional hydrodynamics. *Physica D*, 48: 272–294, 1991.

P. Weiss, D. Oberle, D. W. Meyer, and P. Jenny. Impact of turbulence forcing schemes on particle clustering. *Physics of Fluids*, 31(6):061703, 2019.

M. Wells and G. van Heijst. Dipole formation by tidal flow in a channel. In *International symposium on shallow flows. Balkema Publishers, Delft*, pages 63–70, 2004.

S. Wetchagarun and J. J. Riley. Dispersion and temperature statistics of inertial particles in

isotropic turbulence. *Physics of Fluids*, 22(6):063301, 2010.

C. D. Winant. Three-dimensional residual tidal circulation in an elongated, rotating basin. *Journal of Physical Oceanography*, 38(6):1278–1295, 2008.

Y. Yang, T. F. M. Chui, P. P. Shen, Y. Yang, and J. D. Gu. Modeling the temporal dynamics of intertidal benthic infauna biomass with environmental factors: Impact assessment of land reclamation. *Science of The Total Environment*, 618:439–450, 2018.

M. Yudine. Physical considerations on heavy-particle diffusion. In *Advances in geophysics*, volume 6, pages 185–191. Elsevier, 1959.

E. Zambianchi, M. Trani, and P. Falco. Lagrangian transport of marine litter in the mediterranean sea. *Frontiers in Environmental Science*, 5:5, 2017.

H. Zhang. Transport of microplastics in coastal seas. *Estuarine, Coastal and Shelf Science*, 199: 74–86, 2017.

Q. Zhang and Z. Xiao. Single-particle dispersion in compressible turbulence. *Physics of Fluids*, 30(4):040904, 2018.

Z. Zhang and H. H. Savenije. The physics behind van der burgh's empirical equation, providing a new predictive equation for salinity intrusion in estuaries. *Hydrology and Earth System Sciences*, 21(7):3287–3305, 2017.

S. Zhiyao, W. Tingting, X. Fumin, and L. Ruijie. A simple formula for predicting settling velocity of sediment particles. *Water Science and Engineering*, 1(1):37–43, 2008.

J. Zhou, R. J. Adrian, S. Balachandar, and T. Kendall. Mechanisms for generating coherent packets of hairpin vortices in channel flow. *Journal of fluid mechanics*, 387:353–396, 1999.

J. Zimmerman. The tidal whirlpool: a review of horizontal dispersion by tidal and residual currents. *Netherlands Journal of Sea Research*, 20(2-3):133–154, 1986.